

Linear Wind-Forced Beta Plumes with Application to the Hawaiian Lee Countercurrent*

ALI BELMADANI,⁺ NIKOLAI A. MAXIMENKO,[#] JULIAN P. MCCREARY,[@] RYO FURUE,[#]
OLEG V. MELNICHENKO,[#] NIKLAS SCHNEIDER,[@] AND EMANUELE DI LORENZO[&]

⁺ *International Pacific Research Center, School of Ocean and Earth Science and Technology, University of Hawai'i at Mānoa, Honolulu, Hawaii, and Department of Geophysics, Faculty of Physical and Mathematical Sciences, Universidad de Concepción, Concepción, Chile*

[#] *International Pacific Research Center, School of Ocean and Earth Science and Technology, University of Hawai'i at Mānoa, Honolulu, Hawaii*

[@] *International Pacific Research Center, and Department of Oceanography, School of Ocean and Earth Science and Technology, University of Hawai'i at Mānoa, Honolulu, Hawaii*

[&] *School of Earth and Atmospheric Sciences, Georgia Institute of Technology, Atlanta, Georgia*

(Manuscript received 3 October 2012, in final form 1 May 2013)

ABSTRACT

Two numerical ocean models are used to study the baroclinic response to forcing by localized wind stress curl (i.e., a wind-forced β plume, which is a circulation cell developing to the west of the source region and composed of a set of zonal jets) with implications for the Hawaiian Lee Countercurrent (HLCC): an idealized primitive equation model [Regional Ocean Modeling System (ROMS)], and a global, eddy-resolving, general circulation model [Ocean General Circulation Model for the Earth Simulator (OFES)]. In addition, theoretical ideas inferred from a linear continuously stratified model are used to interpret results. In ROMS, vertical mixing preferentially damps higher-order vertical modes. The damping thickens the plume to the west of the forcing region, weakening the near-surface zonal jets and generating deeper zonal currents. The zonal damping scale increases monotonically with the meridional forcing scale, indicating a dominant role of vertical viscosity over diffusion, a consequence of the small forcing scale. In the OFES run forced by NCEP reanalysis winds, the HLCC has a vertical structure consistent with that of idealized β plumes simulated by ROMS, once the contribution of the North Equatorial Current (NEC) has been removed. Without this filtering, a deep HLCC branch appears artificially separated from the surface branch by the large-scale intermediate-depth NEC. The surface HLCC in two different OFES runs exhibits sensitivity to the meridional wind curl scale that agrees with the dynamics of a β plume in the presence of vertical viscosity. The existence of a deep HLCC extension is also suggested by velocities of Argo floats.

1. Introduction

a. Background

1) DEFINITION OF A β PLUME

A β plume (Rhines 1994) is the anisotropic large-scale ocean circulation induced by a localized vorticity source (associated with fluxes of momentum, heat, or mass). The basic dynamics of β plumes can be described with linear models that allow for analytical solutions (Stommel

1982; Pedlosky 1996). In such models, the steady-state response to a localized patch of wind curl is a zonally elongated gyre consisting of a pair of zonal jets extending to the west of the forcing region, which is established by the westward radiation of barotropic and baroclinic Rossby waves.

2) SMALL-SCALE PATCHES OF WIND CURL

Compact vorticity sources arising from small-scale wind stress curl are present in many regions of the World Ocean (Chelton et al. 2004). They can appear at the oceanic mesoscale as a result of air–sea interaction over SST fronts (e.g., Small et al. 2008), surface currents (Cornillon and Park 2001; Kelly et al. 2001), or from orographic effects near coastlines and islands (Xie et al. 2001; Jiménez et al. 2008). The resulting patterns of small-scale wind curl differ markedly, from monopoles (e.g., next to the coast) and dipoles (e.g., next to an

* International Pacific Research Center/School of Ocean and Earth Science and Technology Publication Number 990/8955.

Corresponding author address: Ali Belmadani, DGEO, FCFM, Universidad de Concepción, Avda. Esteban Iturra s/n - Barrio Universitario, Casilla 160-C, Concepción, Chile.
E-mail: abelmadani@dgeo.udec.cl

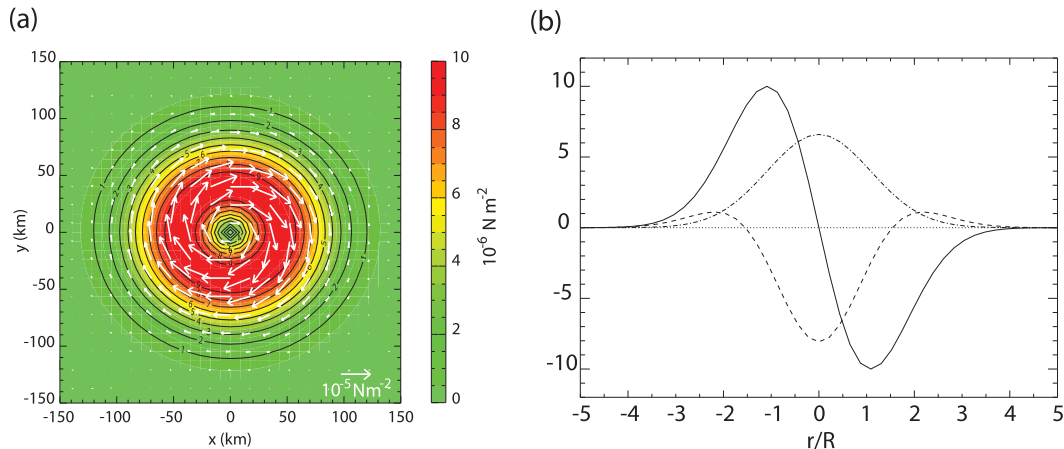


FIG. 1. (a) Surface wind stress [10^{-6} N m^{-2} ; contour interval (CI) = 10^{-6} N m^{-2}] with max at $R = 40 \text{ km}$ (location indicated by the meridionally stretched red circle in Fig. 2a) applied in the box marked in Fig. 2a. (b) Azimuthal wind stress (10^{-6} N m^{-2} ; solid line) and associated wind stress curl ($10^{-10} \text{ N m}^{-3}$; dashed line) and Gaussian streamfunction (10^{-1} N m^{-1} ; dashed-dotted line) as a function of radial distance divided by R .

island) to more complicated structures (e.g., in the Southern Ocean), on horizontal scales of 10–1000 km (Chelton et al. 2004). It has been hypothesized that the Hawaiian Lee Countercurrent (HLCC; Qiu et al. 1997) may be interpreted as a prominent example of a β plume forced by such winds: the tall volcanoes of the island of Hawaii block the trade winds, inducing a small-scale wind stress–curl dipole downstream of the island; it generates the narrow near-surface HLCC, which flows eastward against the large-scale westward North Equatorial Current (NEC; Xie et al. 2001).

3) PREVIOUS STUDIES

Previous studies of β -plume dynamics have used barotropic (Haidvogel and Rhines 1983; Waterman and Jayne 2012), reduced-gravity (Davey and Killworth 1989; Özgökmen et al. 2001), or other simplified models with a small number of vertical layers (Spall 2000; Kida et al. 2008, 2009). Although such models can simulate basic β -plume features, they are not able to simulate its vertical structure realistically because of their limited vertical resolution.

b. Present research

In this paper, we investigate the vertical structure of β plumes using two numerical models: the Regional Ocean Modeling System (ROMS; Shchepetkin and McWilliams 2005; Haidvogel et al. 2008), forced with an idealized, small-scale wind pattern with a quasi-monopole curl; and the Ocean General Circulation Model for the Earth Simulator (OFES; Masumoto et al. 2004). The former model is useful for isolating basic physics, and the latter provides simulations of the HLCC that are

as realistic as possible. To help with the dynamical interpretation of the numerical results, we use theoretical ideas inferred from a linear continuously stratified (LCS) model. Finally, to check the realism of the OFES solutions, we compare them with observations of surface and deep flow derived from trajectories of Argo floats (Lebedev et al. 2007).

2. Models and data

Idealized solutions are obtained using ROMS, which solves the hydrostatic primitive equations with stretched sigma coordinates on 32 vertical levels. ROMS is used at a resolution of $1/12^\circ$ in a closed rectangular subtropical domain (20° – 40°N , 60° zonal extent) with a flat bottom of depth $H = 4000 \text{ m}$. Each run starts from no motion and from horizontally uniform stratification typical for the eastern part of the North Pacific subtropical gyre (Antonov et al. 2010; Locarnini et al. 2010). Subgrid-scale vertical mixing is parameterized by a constant Laplacian viscosity ν of $10^{-4} \text{ m}^2 \text{ s}^{-1}$ and diffusivity κ of $10^{-5} \text{ m}^2 \text{ s}^{-1}$. A 50-km-wide sponge layer is used along the lateral boundaries to resolve the western boundary Munk layer and to damp Kelvin waves. Horizontal viscosity and diffusivity increase linearly within the sponge layer from zero at the interior to $700 \text{ m}^2 \text{ s}^{-1}$ along the solid boundaries. There is no explicit horizontal mixing outside the sponge layer; the model relies on a third-order upstream-biased advection operator for horizontal mixing.

The idealized model is forced at the surface with a steady anticyclonic wind vortex generated by a Gaussian streamfunction located in the center of the domain

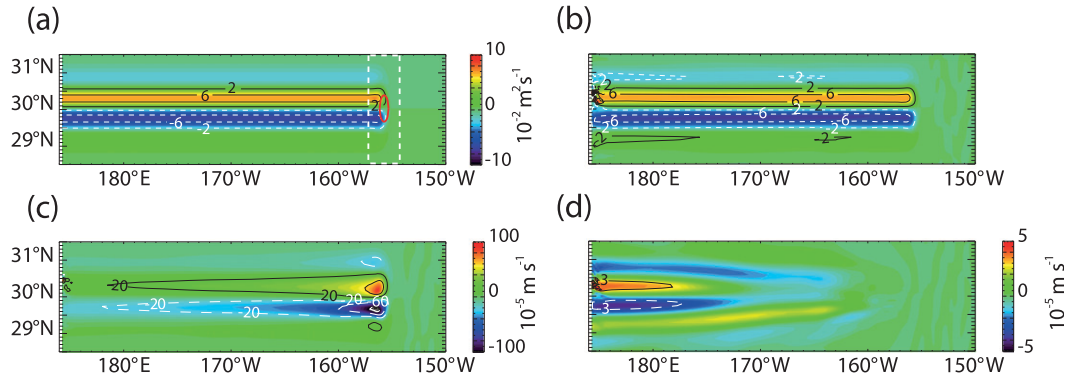


FIG. 2. (a),(b) Steady-state barotropic zonal transport per unit width ($10^{-2} \text{ m}^2 \text{ s}^{-1}$; $\text{CI} = 4.10^{-2} \text{ m}^2 \text{ s}^{-1}$) to the west of the forcing region (a) computed analytically and (b) from ROMS. (c),(d) Zonal current from ROMS (10^{-5} m s^{-1}) at sea surface ($\text{CI} = 4.10^{-4} \text{ m s}^{-1}$) in (c) and at 564-m depth ($\text{CI} = 6.10^{-5} \text{ m s}^{-1}$) in (d). The plots have been stretched meridionally for clarity. The red ellipse and the dashed white box in (a) indicate the location of max surface wind stress and the region represented in Fig. 1a, respectively.

(Figs. 1a,b and appendix A), giving a maximum wind stress of $\tau_{\text{max}} = 10^{-5} \text{ N m}^{-2}$ at a distance $R = 40 \text{ km}$ from the vortex center, which corresponds to a typical value for the deformation radius of the first baroclinic mode at 30°N in the eastern Pacific (Chelton et al. 1998). Such a weak forcing ensures that the model remains in a linear regime, that is, the horizontal advection terms are insignificant and the formation of eddies is prevented. The associated curl consists of a negative central region surrounded by a weaker positive ring, a quasi-monopole (Fig. 1b and appendix A). Because the system is linear, the response to an arbitrary compact forcing (dipole, band, etc.) can be expressed as a linear combination of the responses to monopoles of this sort. Heat and freshwater fluxes are set to zero. The time step of the integration is 20 min for the baroclinic response and 20 s for the barotropic mode. Simulations are run for 10 years after a 20-yr spinup, by which time they are close to a steady state.

The baroclinic structure of the HLCC is investigated by analyzing two solutions to OFES as well as currents estimated from Argo data. OFES is a global eddy-resolving (0.1°) model with 54 vertical levels and with vertical mixing parameterized using the K -profile parameterization (KPP) scheme (Large et al. 1994). As in Sasaki and Nonaka (2006), we compare OFES simulations forced by the National Centers for Environmental Prediction (NCEP)–National Center for Atmospheric Research (NCAR) reanalysis (Kalnay et al. 1996) winds (OFES-N) and by the Quick Scatterometer (QuikSCAT) satellite winds (OFES-Q), offering more spatial details, for the time period 1999–2008. Observed surface and deep ($\sim 1000 \text{ m}$) HLCC velocities are estimated from trajectories of 4284 Argo floats over 1997–2007, bin averaged on a global 1° grid (YoMaHa'07 data; Lebedev

et al. 2007). In addition to mean velocities, the dataset contains values of standard deviation and data density. Uncertainties in the velocity estimates are substantial and are discussed in appendix B.

3. Results

a. Idealized β plume

The strength of the linear, inviscid β plume is set by the Sverdrup balance (Sverdrup 1947),

$$\beta \frac{\partial \Psi}{\partial x} = \mathbf{k} \cdot \frac{\nabla \times \boldsymbol{\tau}}{\rho_b}, \quad (1)$$

where β is the meridional gradient of the Coriolis parameter f , Ψ is the barotropic streamfunction, $\boldsymbol{\tau}$ is the surface wind stress, and ρ_b is the average density of the water column in the study region. As shown in appendix A, the barotropic circulation that forms in response to the localized anticyclonic wind vortex [(A3)] consists of three β -plume cells: a main anticyclonic cell aligned with the vortex center and two weaker cyclonic cells on its flanks (Fig. 2a). Four zonal jets, fringing these cells, extend from the forcing area to the western boundary. Because (1) holds outside the sponge layer along the western boundary, the barotropic flow of the numerical solution (Fig. 2b) agrees well with the analytical solution (Fig. 2a). To the west of the forcing region, the flow is purely zonal and independent of longitude in accordance with (1).

Unlike the barotropic transport, the surface jets decay westward (Fig. 2c). The decay is due to the momentum redistribution between the upper ocean and the interior. Indeed, the bottom of the main eastward jet deepens with distance from the source, leading to the emergence

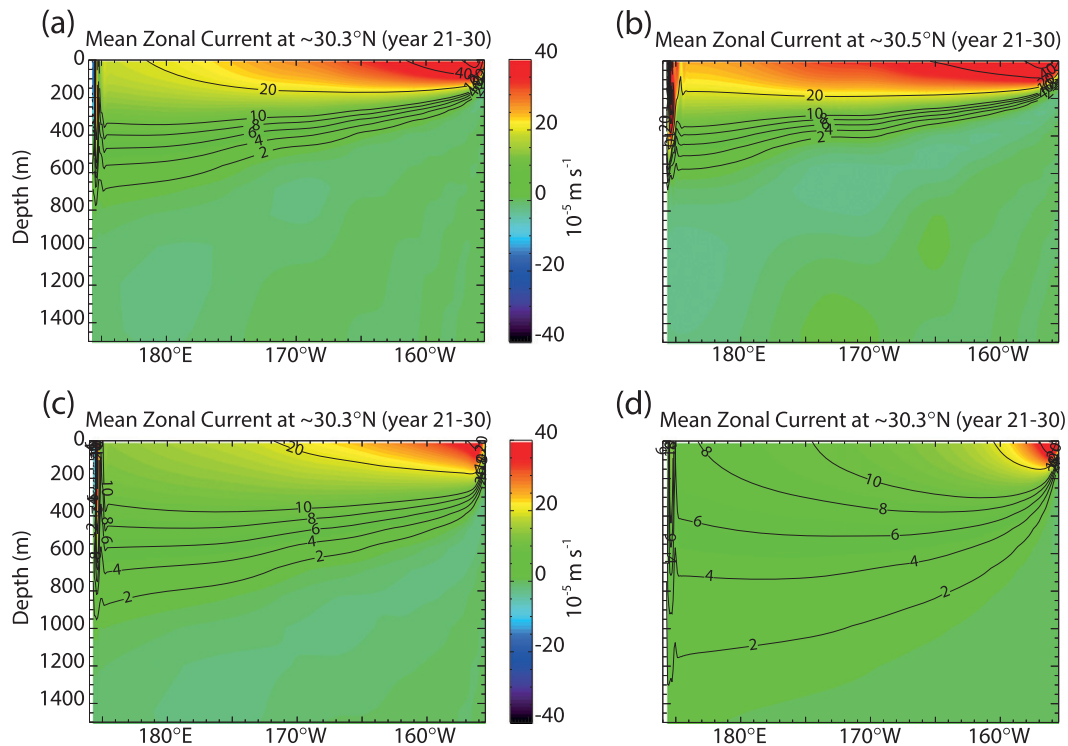


FIG. 3. Steady-state zonal current along the main eastward jet axis from ROMS [10^{-5} m s^{-1} ; $\text{CI} = 2.10^{-5} \text{ m s}^{-1}$ ($2.10^{-4} \text{ m s}^{-1}$) for values below 10^{-4} m s^{-1} (above $2.10^{-4} \text{ m s}^{-1}$); values below $2.10^{-5} \text{ m s}^{-1}$ are not contoured] with (a) $\kappa = 10^{-5} \text{ m}^2 \text{ s}^{-1}$, $\nu = 10^{-4} \text{ m}^2 \text{ s}^{-1}$, and $R = 40 \text{ km}$; and (b) $R = 80 \text{ km}$. Note that the jet axis is shifted northward by 0.2° in (b) as a consequence of the broader wind forcing projected onto the model grid. (c), (d) As in (a), but for $\kappa = 10^{-4} \text{ m}^2 \text{ s}^{-1}$ in (c) and $\nu = 10^{-3} \text{ m}^2 \text{ s}^{-1}$ in (d).

of deep flow far from the forcing region (Fig. 3a; see also Fig. 2d) and to a reduction in vertical shear.

b. Application to the HLCC

1) OFES SOLUTIONS

Similar to the idealized β plume (Fig. 2c), the HLCC surface flow features a westward decay in both OFES simulations (Figs. 4a,b; see also Figs. 8c,d, described in greater detail below). A notable difference between the two solutions is the HLCC zonal extent: whereas the surface HLCC does not appear to extend beyond $\sim 175^\circ\text{W}$ in OFES-Q (Fig. 4b), in agreement with surface drifter data (Qiu et al. 1997; Yu et al. 2003; Lumpkin and Flament 2013), it extends much farther west in OFES-N, as evident in the patches of eastward current found along the HLCC axis between 150° and 155°E and the date line (Fig. 4a). As shown in section 4, these differences may be partly because of the horizontal scale of the forcing.

Regarding the vertical structure of the flow to the west of Hawaii along the HLCC axis, both simulations have the eastward-flowing HLCC in the upper $\sim 200\text{-m}$ depth

with maximum velocities of $6\text{--}8 \text{ cm s}^{-1}$; it lies on top, and to the east, of the westward-flowing NEC, which extends down to $\sim 600\text{-m}$ depth, with maximum velocities exceeding 10 cm s^{-1} near the western boundary and with weaker currents of $1\text{--}2 \text{ cm s}^{-1}$ to the east of 170°E (Figs. 5a and 6a). These results are in agreement with the geostrophic velocities derived between 170°E and 160°W by Yoshida et al. (2011) from Argo hydrographic data over 2005–09. Note that the HLCC core is located below the surface at $\sim 30\text{-m}$ depth in both simulations and tends to extend farther west compared to its surface signature (see the thin layer of near-surface westward flow in Figs. 5a and 6a), to $130^\circ\text{--}140^\circ\text{E}$ for OFES-N and $140^\circ\text{--}150^\circ\text{E}$ for OFES-Q (horizontal maps not shown) instead of $150^\circ\text{--}155^\circ\text{E}$ for OFES-N and $\sim 175^\circ\text{W}$ for OFES-Q at the surface (Fig. 4); this westward extent is in agreement with the hydrographic data of Kobashi and Kawamura (2002) and of Aoki et al. (2002), which indicate the presence of the HLCC to the west of the date line.

On the other hand, the OFES simulations have a weak ($0.5\text{--}1 \text{ cm s}^{-1}$) eastward flow below the NEC (Figs. 5a and 6a), which is absent from previous observational

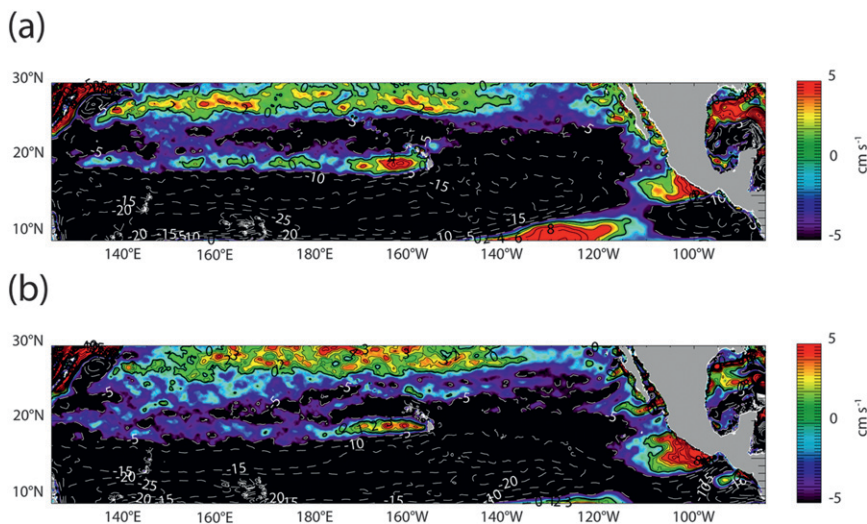


FIG. 4. Time-mean surface zonal current (cm s^{-1}) from (a) OFES-N and (b) OFES-Q over 1999–2008. Solid (dashed) contours are for eastward (westward) current. The thick solid contours are for zero velocity. CI is 5 cm s^{-1} for westward flow and (a) 2 cm s^{-1} and (b) 1 cm s^{-1} for eastward flow. Note the differences in the HLCC zonal extent between the two model solutions.

studies that lack deep flow observations. In OFES-N, this deep current seems to originate a few degrees to the west of the Hawaiian Islands, underneath the HLCC at its location of maximum velocity, and deepens toward the west; for example, the 0.5 cm s^{-1} contour reaches depths of 1000–1200 m near 140°E (Fig. 5a). In OFES-Q, the two currents are separated by westward flow near $\sim 163^\circ\text{W}$ (Fig. 6a). The subsurface eastward current appears to continue to the east of Hawaii and to shoal until it reaches the near surface at the basin eastern boundary, near the coast of Mexico in both simulations (Figs. 5a and 6a), challenging the hypothesis of an island-induced flow. Still, there is a clear step in the deep flow magnitude in OFES-N, from $0\text{--}0.5 \text{ cm s}^{-1}$ to the east of Hawaii to $0.5\text{--}1 \text{ cm s}^{-1}$ to the west of the islands (Fig. 5a), which suggests a contribution of the HLCC β plume. Although not as marked, there is also a jump in OFES-Q (Fig. 6a), as indicated by the vertical extent of the 0.5 cm s^{-1} closed contours that is smaller to the east ($\sim 150 \text{ m}$) compared to the west ($\sim 400 \text{ m}$) of the islands.

In fact, the connection between the deep flow and the surface HLCC in both OFES simulations is best revealed by removing the large-scale NEC flow. Indeed, to extract the narrow HLCC signal from the OFES-N (OFES-Q) solution, we isolate it from the broad NEC using a high-pass filter in y with a Hann window of 10° (6°) half-width. This filtering allows for the HLCC to be compared more easily to the idealized experiments presented in section 3a, which do not contain

any background flow. The different filter widths chosen for the two OFES solutions are related to the different HLCC meridional scales, which are related to different scales of the wind products (see below).

High-pass-filtered zonal currents reproduce the main characteristic features of the idealized baroclinic β plumes (Figs. 5c and 6c): westward reduction in vertical shear, decay of surface flow (see also Figs. 8c,d, described in greater detail below), emergence of deep flow (extending down to 1000–1200 m as indicated by the 0.5 cm s^{-1} contours in Figs. 5c and 6c) to the west of the island (see also Fig. 7b), and (in OFES-N) westward deepening of the eastward flow (evidenced by the 0.5 cm s^{-1} and 1 cm s^{-1} contours in Fig. 5c). Note the similarity of the high-pass-filtered and unfiltered deep flows on Figs. 5 and 6, which reflects the absence of large-scale flow below $\sim 600 \text{ m}$ (Figs. 5b and 6b) and excludes the possibility that the deep flow may be an artifact of spatial filtering. However, the NEC signal is not removed completely at intermediate depths, as can be seen in Figs. 5c and 6c from a layer of lower eastward velocities around 400-m depth (veering westward near the Asian coast), extending roughly from the western boundary to the date line. This limits to some extent our interpretation, although the striking similarity between the ROMS and OFES-N model results suggests it is not a critical issue.

In OFES-Q, the deep flow appears to achieve its maximum directly below or possibly even to the east of the maximum near-surface flow and remains at

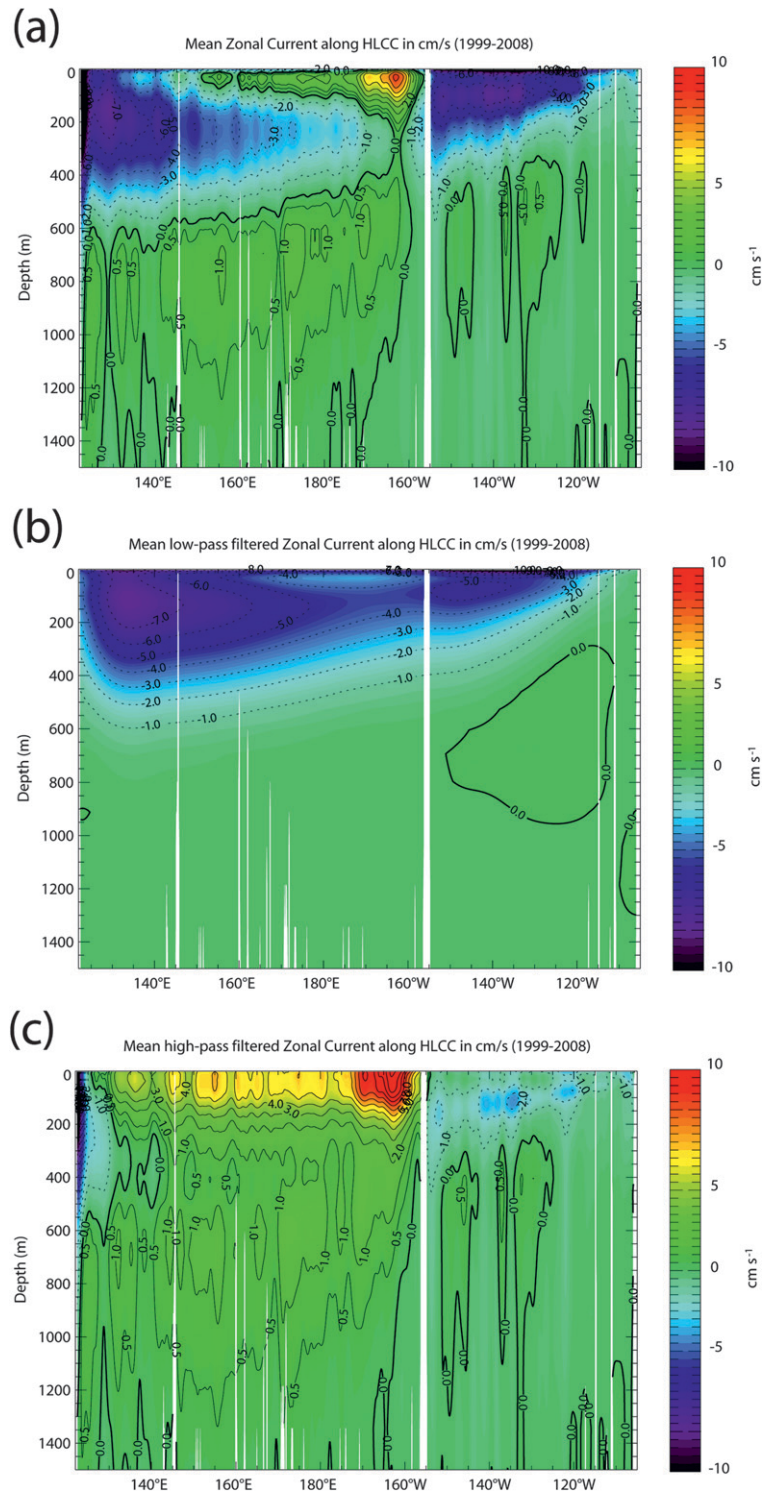


FIG. 5. (a) Zonal current along the HLCC axis in OFES-N, time-averaged over 1999–2008 and meridionally averaged between 18° and 20°N (cm s^{-1} ; $\text{CI} = 1 \text{ cm s}^{-1}$; with 0.5 cm s^{-1} contour plotted and thick solid contours for zero velocity). (b),(c) As in (a), but after applying meridional low-pass filter in (b) and high-pass filter in (c) (Hann window, see text). The Hawaii Island (Mexico) west coast is located at 156°W (107°W). Once isolated from the large-scale NEC that dominates zonal flow at intermediate depths, the HLCC appears to have a vertical structure consistent with the idealized β plume, which includes a deep extension.

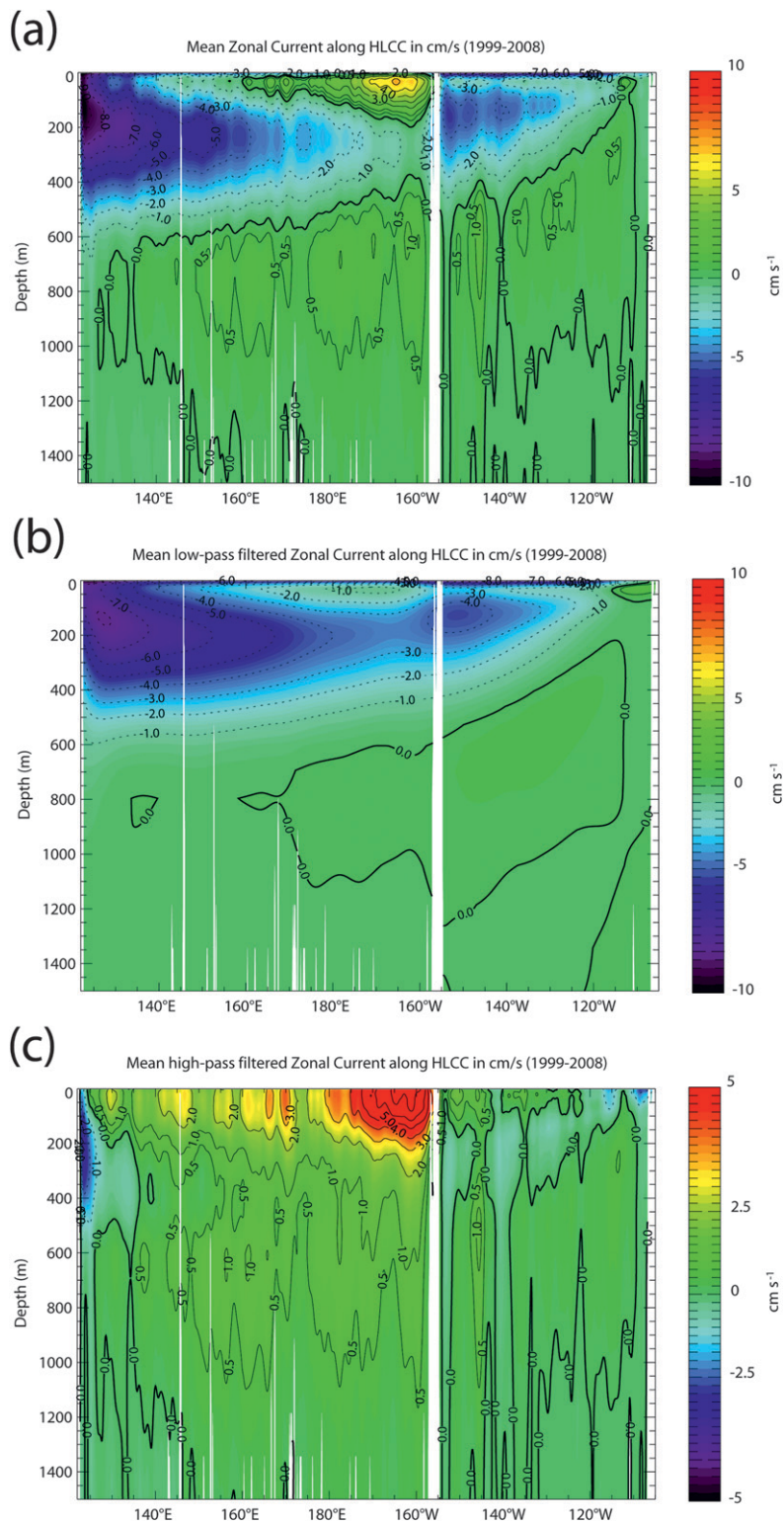


FIG. 6. As in Fig. 5, but for OFES-Q averaged meridionally between the thick dashed lines in Figs. 7a,b. The transect was chosen to match the axis of the HLCC in OFES-Q. Note the differences in color scales between (c) and Fig. 5c. The near-surface current decay is shorter in OFES-Q compared to OFES-N and the deep eastward flow does not intensify westward.

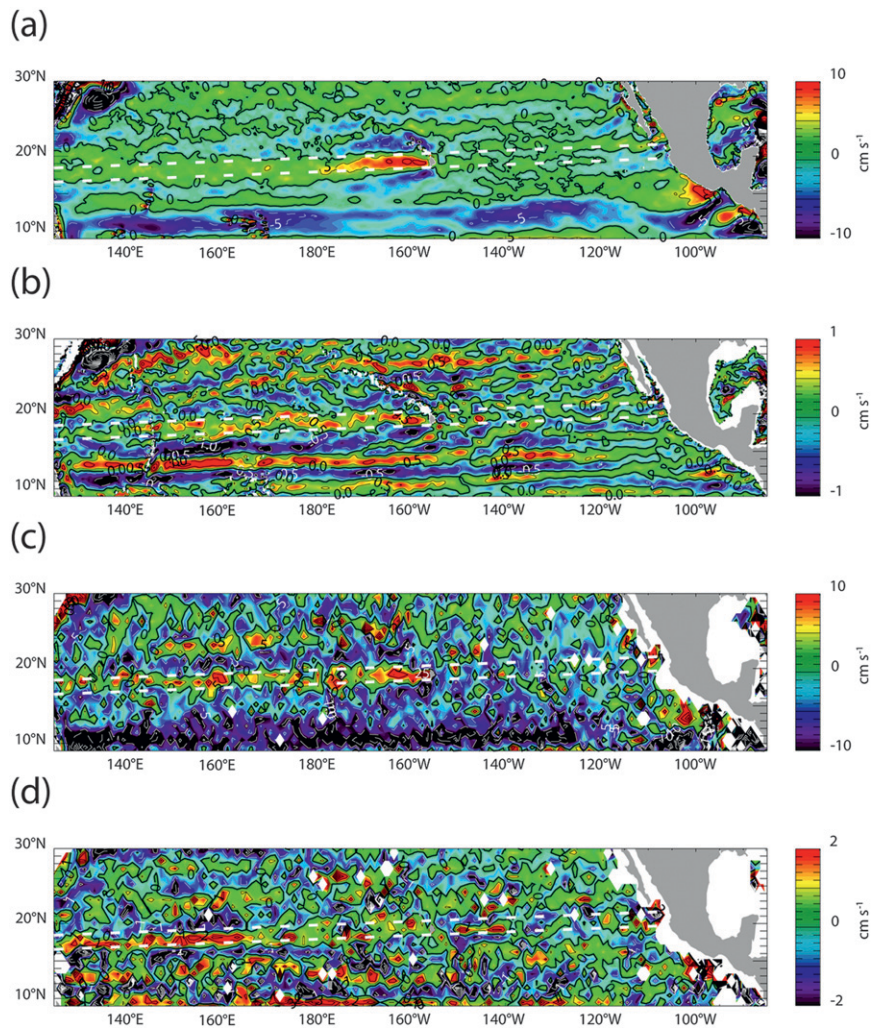


FIG. 7. Meridionally high-pass-filtered (Hann window, see text) time-mean zonal current (cm s^{-1}) (a) at sea surface and (b) at 1041-m depth (hereafter referred to as 1000-m depth) from OFES-Q over 1999–2008. (c),(d) As in (a),(b), but for Argo float velocities (YoMaHa'07) at sea surface in (c) and at 1000-m depth in (d) averaged over 1997–2007. CI are 5 cm s^{-1} in (a),(c), 0.5 cm s^{-1} in (b), and 1 cm s^{-1} in (d). Solid (dashed) contours are for eastward (westward) current. Thick solid contours are for zero velocity. Thick dashed lines in (a),(b) are used to meridionally average OFES-Q data as shown on Fig. 6. Thick dashed lines in (c),(d) are the same as those in (a),(b). The surface flow decay is evident in both OFES-Q outputs and YoMaHa'07 data, but the apparent increasing deep flow to the west of the islands is not represented in the model.

a constant depth far to the west (see the 0.5 cm s^{-1} contour on Fig. 6c; see also Figs. 7a,b), unlike the idealized model. An apparent core of the subsurface eastward flow seems to be deepening when looking at unfiltered data (Fig. 6a), but this is deceptive because this feature is due to the superimposition of the constant-depth deep eastward flow (Fig. 6c) with the deepening westward-flowing NEC (Fig. 6b). Yet, the presence of the subsurface eastward flow seems to be related to the presence of the island and possibly the HLCC. Indeed,

while large horizontal scales show coherent flow structure at all depths across the basin (Fig. 6b), small meridional scales show distinct structures on both sides of the island (Fig. 6c). The eastward flow found to the east of Hawaii that deepens westward is much weaker than its counterpart found to the west of Hawaii and changes sign on multiple occasions, unlike the latter (Fig. 6c). In addition, it is capped by weak westward flow that also deepens westward, but is not found to the west of the island. As expected, any eastward surface flow found to

the east of Hawaii is much weaker than the HLCC. The discrepancy between the deep flows in OFES-Q on the one hand and in both OFES-N and the idealized model on the other hand may be the result of air–sea interaction or nonlinear dynamics (see below).

The figures also reveal that the surface jets extend as far west as $\sim 130^\circ\text{E}$, but are significantly weaker to the west of $\sim 170^\circ\text{W}$ in both runs (Figs. 5c and 6c). This decay is consistent with Sasaki and Nonaka (2006), who reported the HLCC termination in OFES near the date line. Noteworthy is that whereas the maximum eastward velocity of the near-surface HLCC is located at about $\sim 30\text{-m}$ depth in the unfiltered data (Figs. 5a and 6a), it is located at the surface in the meridionally filtered data (Figs. 5c and 6c). In fact, there is a very thin layer of intensified westward flow (purple color) very close to the surface in the low-pass-filtered data (Figs. 5b and 6b). These features are likely due to large-scale near-surface Ekman drift, which has a slight westward component associated with the northeasterly trade winds (not shown). On the other hand, the surface current zonal decay scale is shorter in OFES-Q (Fig. 6c) than in OFES-N (Fig. 5c). This is particularly obvious in horizontal maps of the high-pass-filtered surface flows (Figs. 8c,d).

To further show that the deep eastward flow below the HLCC in OFES-Q is related to the presence of the island and hence likely a deep HLCC extension, horizontal maps of high-pass-filtered surface and deep flows are shown in Figs. 7a and 7b. From these figures, it is clear that while zonally coherent eastward flow is found along the HLCC axis to the west of Hawaii both at the surface and 1000-m depth, no such coherence is found to the east. Some striated pattern resembling features previously found in both observations (Maximenko et al. 2008) and numerical models (Centurioni et al. 2008; Melnichenko et al. 2010) may be seen to the east of the island, but they are weaker, noisier, and not aligned with the HLCC.

Figures 8a and 8b show the 1999–2008 mean barotropic zonal transport per unit width in OFES-N and OFES-Q, respectively, after the high-pass filtering is applied. Consistent with the Sverdrup dynamics, both runs exhibit zonally stretched cyclonic and anticyclonic circulations to the west of the island of Hawaii, aligned with the regions of positive and negative wind stress curl (white contours), respectively; these circulations give rise to the HLCC between them and strengthen the NEC on the outer flanks. The wind stress–curl dipole is much broader and somewhat weaker in the coarse NCEP wind data compared to the higher-resolution QuikSCAT data (Figs. 8a,b), as previously noted by Sasaki and Nonaka (2006). As a result, the HLCC meridional scale is larger for OFES-N ($\sim 3^\circ$) compared to OFES-Q ($\sim 2^\circ$).

One discrepancy between the OFES HLCC and the idealized β plume is the relative decay of the barotropic and surface flows. In the idealized model, the surface flow decays westward, while the barotropic flow extends to the western boundary without decay (Fig. 2). Although stretching over distances of several thousand kilometers, the HLCC barotropic transport decays westward in the OFES simulations, particularly in OFES-Q (Figs. 8a,b; see also Fig. 10, described in greater detail below). In OFES-N, although the barotropic flow drops steeply by $\sim 40\%$ near 165°W , it is nearly zonally uniform between 165°W and 170°E (Fig. 8a), while the surface flow decays by $\sim 60\%$ over the same longitude range (Fig. 8c), similar to the idealized β plume (Fig. 2b). The analogy with the latter is limited to the west of 170°E where the OFES-N barotropic flow encounters a meridionally oriented topographic barrier (not shown) and drops again by $\sim 50\%$ (possibly as a result of topographic steering and associated vortex stretching, which are not represented in the idealized model), while the surface flow appears undisturbed (Figs. 8a,c). In contrast, in OFES-Q both the zonal transport of the HLCC and the surface flow decay westward from about 160°W to 180° with approximately the same rate and are slightly tilted southwestward (Figs. 8b,d). As shown below, the former feature is likely due to the QuikSCAT wind stress curl pattern and underlying air–sea interaction in the far field, which is absent in the NCEP data (Xie et al. 2001; Sasaki and Nonaka 2006), while the latter feature may be the result of nonlinear stress, including eddy fluxes.

Two processes contributing to the barotropic flow but not represented in the idealized model may be responsible for the discrepancy between the OFES and ROMS solutions. On the one hand, nonzero wind stress curl forcing to the west of Hawaii can modify the Sverdrup flow in the far field (Xie et al. 2001). On the other hand, the HLCC is dominated by mesoscale eddies (Holland and Mitchum 2001; Calil et al. 2008; Yoshida et al. 2010; Jia et al. 2011), which may contribute to its early termination via horizontal mixing (Yu et al. 2003) and/or vertical momentum transfer due to eddy form stress, which are not taken into account here.

The eddy kinetic energy (EKE) fields of the OFES-N and OFES-Q solutions are represented in Figs. 9a and 9b, respectively. Eddy activity along the HLCC is of the same order in the run forced by QuikSCAT as that in the run forced by NCEP, if not slightly weaker. This property suggests that eddy-induced horizontal mixing may not be responsible for the shorter extent of the barotropic flow in OFES-Q.

Figure 10 represents the total transports to the west of Hawaii in OFES-N and OFES-Q, as well as those computed from the NCEP and QuikSCAT wind stress

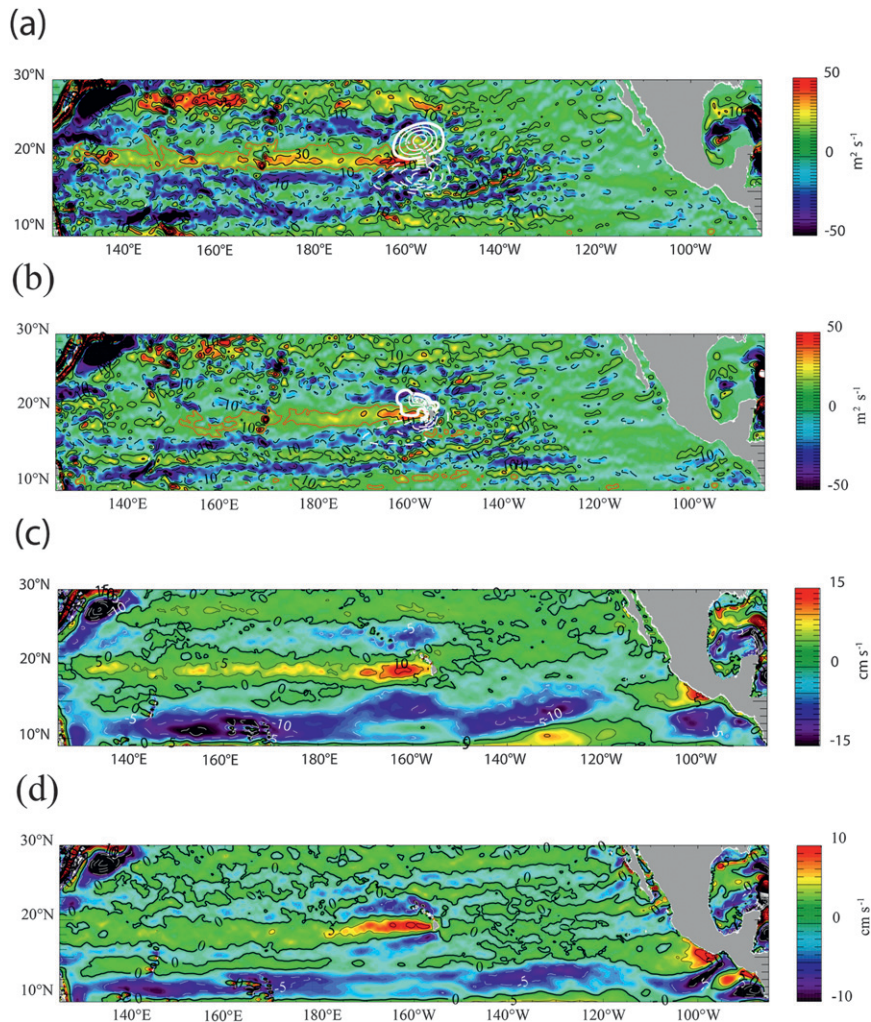


FIG. 8. (a),(b) Meridionally high-pass-filtered (Hann window, see text) time-mean barotropic zonal transport per unit width ($\text{m}^2 \text{s}^{-1}$; $\text{CI} = 20 \text{ m}^2 \text{s}^{-1}$; shading and black contours) and time-mean surface wind stress curl dipole around Hawaii (10^{-7} N m^{-3} ; $\text{CI} = 5.10^{-8} \text{ N m}^{-3}$; white contours), and (c),(d) meridionally high-pass-filtered time-mean surface zonal current (cm s^{-1} ; $\text{CI} = 5 \text{ cm s}^{-1}$) from OFES-N in (a),(c) and OFES-Q in (b),(d) over 1999–2008. Solid (dashed) contours are for eastward (westward) flow. The $10 \text{ m}^2 \text{s}^{-1}$ contours to the west of the islands in (a),(b) are marked in red to indicate the approximate locations of the HLCC. Note the different color scales in (c),(d). The HLCC surface current decay and weaker transport decay in OFES-N are consistent with the idealized β plume. The surface HLCC zonal extent is larger in OFES-N compared to OFES-Q.

curl fields, using the Sverdrup balance [(1)] and the depth-integrated continuity equation [(A4)]. Both the total transports and the wind stress curls have been meridionally high-pass filtered, with the filter characteristics presented earlier, in order to focus on scales relevant to the HLCC barotropic flow and forcing fields. After a sharp increase in the island lee where the forcing is located, the Sverdrup zonal transport per unit width induced by the NCEP winds (thick solid line) increases more progressively between $\sim 165^\circ\text{W}$ and $\sim 160^\circ\text{E}$ before reaching an almost constant value of $\sim 33 \text{ m}^2 \text{s}^{-1}$

farther west. This results from a weak quasi-zonal wake extending the NCEP wind stress curl Hawaii dipole westward to $\sim 160^\circ\text{E}$, and from the absence of coherent small-scale wind structures in the region farther west (not shown). In the absence of small-scale structures in the NCEP coarse-resolution SST forcing, the wind stress curl wake is likely the sole result of the low-level flow perturbation by the Hawaiian orography.

In contrast, the Sverdrup zonal transport per unit width forced by the QuikSCAT winds (thick dashed line on Fig. 10) increases from the island lee to $\sim 170^\circ\text{W}$

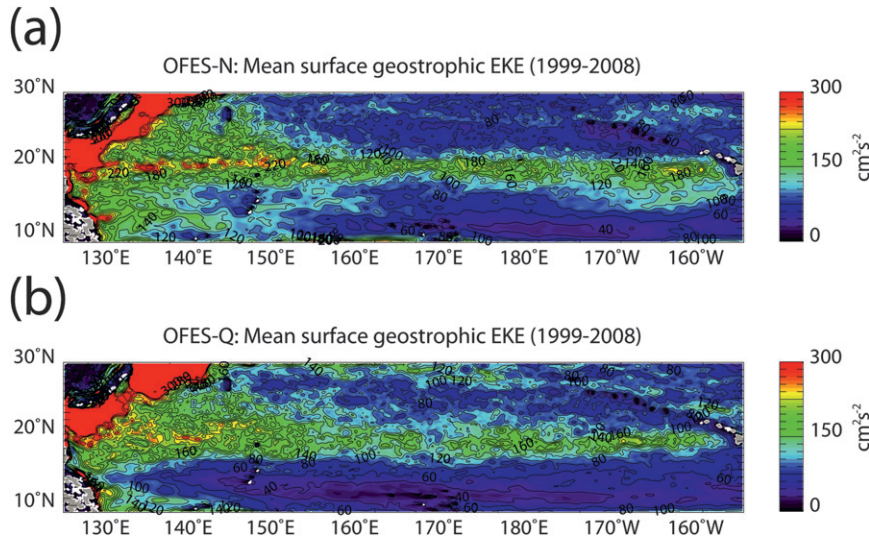


FIG. 9. Time-mean EKE ($\text{cm}^2 \text{s}^{-2}$; $\text{CI} = 20 \text{ cm}^2 \text{s}^{-2}$) over 1999–2008, computed from the surface geostrophic flow for (a) OFES-N and (b) OFES-Q.

where it reaches a maximum of $\sim 43 \text{ m}^2 \text{s}^{-1}$, and then decreases progressively westward by 35%–40%, down to $26\text{--}27 \text{ m}^2 \text{s}^{-1}$ at $130^\circ\text{--}140^\circ\text{E}$. The larger Sverdrup transport in the island lee in OFES-Q is due to the stronger and meridionally narrower wind stress curl compared to OFES-N (Figs. 8a,b). The decrease to the west of $\sim 170^\circ\text{W}$ results from a southwestward shift of the zonally elongated QuikSCAT wind stress–curl dipole (not shown). Hence, at the latitude of the island of Hawaii, both the curl and its meridional gradient change sign rapidly in the westward direction due to this tilt. This implies a westward weakening of Sverdrup zonal transport. The tilt in the curl dipole results partly from air–sea interaction over the HLCC caused by the eastward advection of western Pacific warm waters, which tends to extend the dipole in the far field where the HLCC axis is also tilted meridionally (Xie et al. 2001; Sasaki and Nonaka 2006). Such air–sea coupling over the warm HLCC tongue is not represented in NCEP but is captured by QuikSCAT. However, the linear Sverdrup response itself is not responsible for the tilt in the HLCC because the far-field curl dipole is too weak to generate eastward Sverdrup flow to the south (not shown). Thus, the tilt in the HLCC is likely due to nonlinear stress associated with the background flow, eddies, and/or topographic steering (Kessler et al. 2003).

The total HLCC barotropic transports in OFES-N (thin solid line in Fig. 10) and OFES-Q (thin dashed line) are entirely explained by the Sverdrup response in the island lee until $160^\circ\text{--}165^\circ\text{W}$ where they reach their respective maxima, before decaying westward as a result of nonlinear effects. The faster decay in OFES-Q

appears qualitatively consistent with the wind curl pattern to the west of Hawaii in the QuikSCAT winds, although it is possible that differences in eddy fluxes between the two simulations also play a role. With similar large-scale winds in NCEP and QuikSCAT (not shown) and the same bottom topography in the two OFES runs, it is unlikely that advection by the background flow and topographic steering play any significant role in the faster decay of the OFES-Q barotropic flow.

However, the OFES-Q barotropic flow decreases not only due west but also upstream (southwestward) along the tilted HLCC (Fig. 8b, thin dotted line in Fig. 10). Unlike the region farther north, the transport to the west of $\sim 160^\circ\text{E}$ along the tilted HLCC is directed eastward (cf. thin dashed and dotted lines in Fig. 10). The Sverdrup flow taken along the same tilted axis also decays to the west of $\sim 165^\circ\text{W}$ with a similar, although perhaps slightly faster decay rate (thick dotted line) compared to the total transport (thin dotted line). Compared to the Sverdrup flow taken along the $18.5^\circ\text{--}19.5^\circ\text{N}$ latitude band (thick dashed line), that taken along the tilted HLCC is twice weaker at most and decays faster (thick dotted line). That is because the Sverdrup flow is almost purely zonal and flows westward south of $\sim 18.5^\circ\text{S}$ (not shown). Thus, the slightly faster decay along the tilted HLCC compared to total transport suggests that nonlinear stress may be responsible for the tilt and may act to reduce the decay induced by the far-field small-scale wind pattern. Further studies will be needed in order to test this hypothesis.

The baroclinic β plume generated by the QuikSCAT curl pattern to the west of Hawaii that is acting in

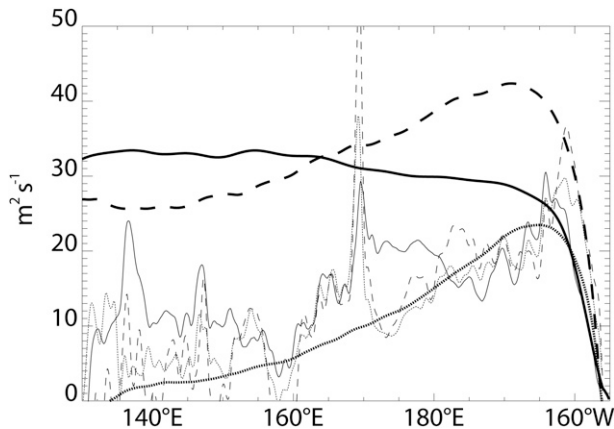


FIG. 10. Sverdrup zonal transport per unit width derived from the meridionally high-pass-filtered (Hann window, see text) time-mean wind forcing fields over 1999–2008, averaged meridionally between 18° and 21° N and between 18.5° and 19.5° N for OFES-N (thick solid line) and OFES-Q (thick dashed line), respectively. Total meridionally high-pass-filtered time-mean zonal transport per unit width over 1999–2008, averaged meridionally between 18° and 21° N and between 18.5° and 19.5° N for OFES-N (thin solid line) and OFES-Q (thin dashed line), respectively. The lat ranges are chosen to capture the HLCC signal in the OFES-N and OFES-Q Sverdrup flows. The Sverdrup and total OFES-Q transports are also averaged meridionally between the thick dashed lines on Figs. 7a,b (thick and thin dotted lines, respectively). Units are $\text{m}^2 \text{s}^{-1}$. Only eastward transports are represented. For simplicity, the eastern limit of the zonal integration used in the Sverdrup calculation is taken as 155° W, thereby ignoring the winds to the east of the islands, and the presence of islands is also ignored.

opposition to the dipole in the island lee may partially cancel the deep eastward flow below the HLCC. This may explain the different vertical structure of the HLCC in OFES-Q (Fig. 6c) compared to that in OFES-N (Fig. 5c). On the other hand, it is also possible that the differences in nonlinear stress between the two simulations, eddy fluxes in particular, play a role in these differences in the baroclinic flow structure.

2) OBSERVATIONS

The YoMaHa'07 ensemble-mean zonal velocities, derived from trajectories of Argo floats and filtered with the high-pass filter used for OFES-Q, are used to assess the observed HLCC vertical structure. Whereas the surface jet is strongest in the lee of Hawaii (Fig. 7c), the deep current there is weak but appears to the west of $\sim 165^{\circ}$ E as a quasi-zonal jet extending 15° – 20° in the zonal direction (Fig. 7d). Despite the large error in deep velocity estimates (Fig. B2c), the presence of a coherent zonal band in the deep flow standard deviation between 140° and 175° E (Fig. B2b) suggests that the deep eastward flow aligned with the surface HLCC axis is not a sampling artifact. The data appear qualitatively consistent

with the idealized model (Figs. 2c,d), with a surface flow decay and a deep flow strengthening in the westward direction (Figs. 7c,d), which may be a deep extension of the HLCC. However, as one might expect given all the limitations of the YoMaHa'07 data (appendix B), the quantitative agreement between the deep flows in YoMaHa'07 and OFES-Q is poor and the comparison is complicated by noise and multiple local maxima (Figs. 7b,d). It should be noted in particular that interpolation artifacts in the YoMaHa'07 data may introduce noise in the meridionally high-pass-filtered velocity fields, which are least constrained in the interpolation originally designed to capture large-scale features (Lebedev et al. 2007).

To allow a sharper comparison of the HLCC vertical structure in OFES-Q and YoMaHa'07, enlargements of the spatially filtered surface and deep zonal currents already shown in Fig. 7 are presented in Fig. 11. Despite the large observational noise, the model and observations are generally in good qualitative agreement at the surface in terms of typical amplitudes in the island lee (8 – 10 cm s^{-1} to the east of 170° W) and location of the HLCC and associated westward jets, with a clear decay and southward shift in the upstream (westward) direction (Figs. 11a,b). The simulated currents in the far field are, however, roughly twice weaker than the observed (typically 2 – 3 cm s^{-1} and 4 – 6 cm s^{-1} to the west of 170° E, respectively) and tend to be broader than the observed estimates. This suggests a stronger decay in the model, although the low signal-to-noise ratio of the YoMaHa'07 data does not allow the drawing of any firm conclusions. On the other hand, the observed deep eastward jet appears to strengthen to the west of $\sim 170^{\circ}$ E and is stronger than the modeled counterpart there (which may be partly related to temporal sampling—see appendix B), whereas the modeled one is more zonally uniform with a few meanders (Figs. 11c,d). Moreover, the observed flow is patchier and less continuous to the east of $\sim 170^{\circ}$ E. Despite these differences, the coincidence of their positions and zonal orientations is remarkable, although with a potentially large error in the YoMaHa'07 flow field (appendix B), their correspondence is not conclusive.

It is also worth noting that the qualitative consistency with the idealized model results does not prove unequivocally that the far-field deep jet-like velocities are the result of the β -plume dynamics described in this study. Indeed, it is possible that the mean deep eastward flow maximum near 160° E is simply associated with the surface flow maximum at the same longitude (Figs. 7c,d and 11b,d), both being signatures of energetic mesoscale eddies for instance. However, this hypothesis appears less likely because far-field surface and deep flows are

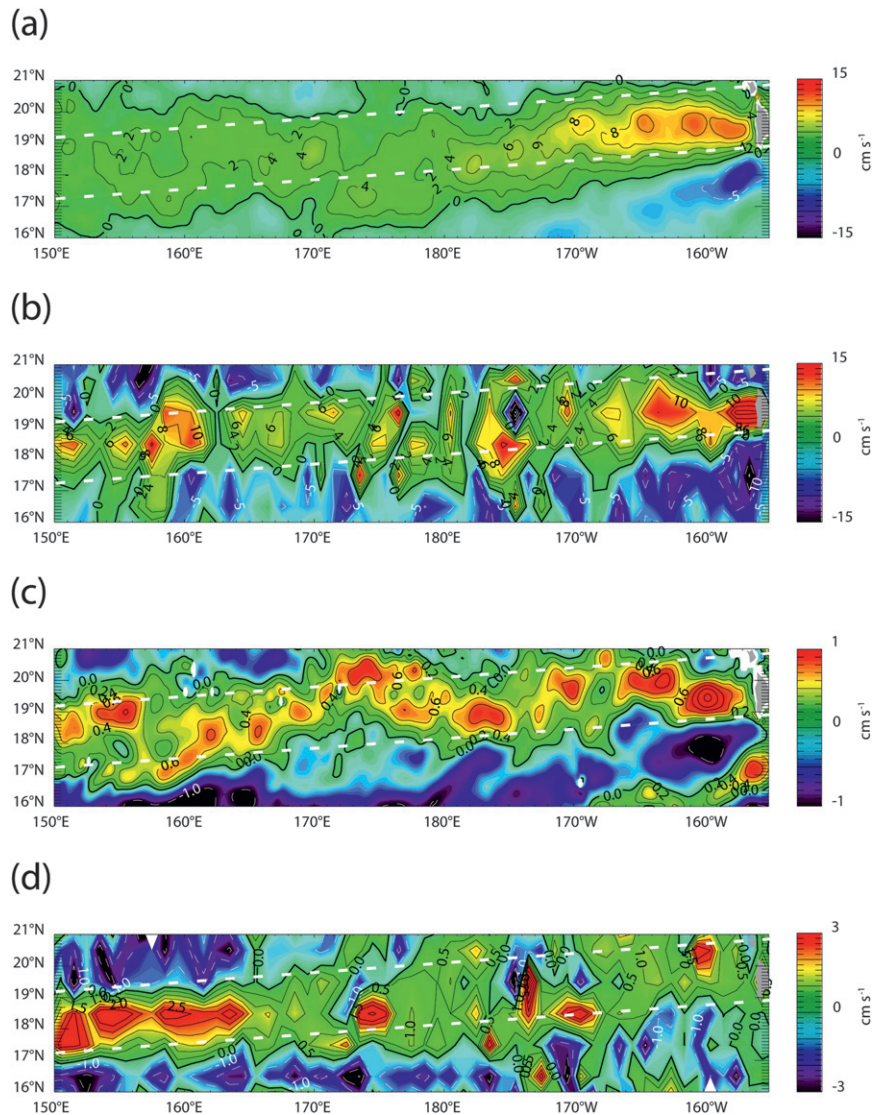


FIG. 11. Comparison of meridionally high-pass-filtered (Hann window, see text) time-mean zonal velocities between OFES-Q averaged over 1999–2008 and Argo float velocities averaged over 1997–2007 (YoMaHa'07). Surface velocity from OFES-Q in (a) and YoMaHa'07 in (b); 1000-m velocity from OFES-Q in (c) and YoMaHa'07 in (d). (a),(b) As in Figs. 7a,c, but enlarged over the region (16° – 21° N, 150° E– 155° W), with a color scale over the broader (-15 cm s^{-1} , 15 cm s^{-1}) range and with CI reduced to 2 cm s^{-1} for eastward velocities lower than 10 cm s^{-1} . (c),(d) As in Figs. 7b,d, but enlarged over the region (16° – 21° N, 150° E– 155° W), with a color scale over the broader (-3 cm s^{-1} , 3 cm s^{-1}) range in (d) and with CI reduced to 0.2 cm s^{-1} for eastward velocities in (c), 0.5 cm s^{-1} for eastward velocities lower than 3 cm s^{-1} in (d).

poorly correlated: unlike the mean deep flow, the mean surface flow does not feature a zonally coherent band of elevated velocities at 145° – 165° E, but a rather patchy structure (Figs. 7c,d, and 11b,d). The same conclusion holds for the spatially high-pass-filtered maps of zonal current standard deviation at the surface (not shown) and at 1000 m (not shown but essentially identical to Fig. B2b, described in greater detail in the appendix,

because of the absence of deep large-scale flow). Another possibility is that the far-field surface and/or deep jets may be associated to striations unrelated to the island-induced wind stress curl forcing. Although plausible given the ubiquity of quasi-zonal jet-like structures (Maximenko et al. 2008), including some clear signals seen closer to the equator in both model and Argo data (Figs. 7b,d), this explanation seems unlikely because

the far-field jets are located along the axis of the surface HLCC. In addition, unlike the OFES-Q outputs, the YoMaHa'07 data show no evidence of such striations to the east of the islands, which is probably because they are weak and somewhat noisy even in altimetric data (Maximenko et al. 2008). This casts doubt on whether such weak signals may leave such a clear signature in the time-mean deep flow to the west of Hawaii (Fig. 7d). Besides, the deep tropical jets are zonally coherent across the whole basin in both YoMaHa'07 and OFES-Q (Figs. 7b,d), unlike the deep jet to the west of Hawaii. Noteworthy, the far-field deep jet at 145°–165°E appears as perhaps the most clearly defined extratropical quasi-zonal jet at 1000-m depth in the YoMaHa'07 dataset globally (Ascani et al. 2010; their Fig. 2).

To the best of our knowledge, a deep HLCC extension, reaching 1000-m depth, has not been discussed previously, although fragmentary hints on such deepening can be found in published material. For example, in situ data collected along meridional transects to the west of Hawaii show a westward deepening of the HLCC (Qiu and Durland 2002), although these observations are limited to two sections conducted at 165°W (in September–November 1994) and 179°E (in July–August 1993) and do not extend below 250-m depth. In addition, a deep (450–1100 m) HLCC extension was also found in a 4½-layer model by McCreary et al. (2007).

4. Theory

The westward reduction in vertical shear, which takes place in both the idealized β -plume simulations and the HLCC, suggests a possible damping of baroclinic Rossby waves with a preference for higher-order vertical modes. Without nonlinearities in the ROMS model, such damping must be from vertical mixing of density (diffusion κ) or momentum (viscosity ν) or both. A test run with κ increased by an order of magnitude, shows that the flow vertical structure is indeed sensitive to κ (Fig. 3c): changes in the zonal direction take place over much shorter distances than in the control run (Fig. 3a). On the other hand, the baroclinic flow is even more sensitive to ν (Fig. 3d): zonal scales are smaller when viscosity is increased by a factor of 10 than when diffusion is increased by a factor of 10 (Fig. 3c). Other experiments in which κ and ν are separately reduced by a factor of 10 exhibited consistent results, that is, larger zonal scales for the baroclinic flows, especially when viscosity is reduced (not shown). Thus, the model is sensitive to mixing strength for a realistic range of values, and so it suggests that both vertical viscosity and diffusion may have important effects on the flow structure in the real ocean. Given that vertical viscosity is not usually important for

the large-scale ocean circulation below the Ekman layer, such strong sensitivity to viscosity is surprising.

An LCS model (e.g., McCreary 1981; appendix C) provides a useful framework for understanding the basic properties of our solutions. In this model, solutions are represented as expansions in a complete set of barotropic and baroclinic modes. For our purposes, the key simplifying assumptions are that the background Väisälä frequency N depends only on z , and that

$$\nu = A/N^2 \quad \text{and} \quad \kappa = A/(\sigma N^2), \quad (2)$$

where $\sigma = \nu/\kappa$ is the Prandtl number and A is a constant, so that the mixing coefficients vary with depth. Because ν and κ are constant in our numerical solutions, we evaluate the LCS equations for constant N , using a typical value in the interior ocean (e.g., 10^{-4} s^{-1} for the subtropical North Pacific).

Solving (C9) for a single equation in p_n alone gives the quasigeostrophic potential vorticity equation (appendix C)

$$\frac{\nu N^2}{c_n^2}(p_{nxx} + p_{nyy}) - \frac{\kappa N^2 f^2}{c_n^4} p_n + \beta p_{nx} = \rho_b f (G_{nx} - F_{ny}), \quad (3)$$

where p_n is the expansion coefficient of the pressure p , c_n is the phase speed of the n th mode gravity wave, F_n and G_n describe how zonal and meridional wind stress couple to each mode, and subscripts x and y indicate a partial derivative with respect to x and y , respectively. Solutions to (3) provide the p_n field of the β plume forced by the winds.

The ν and κ terms on the left-hand side of (3) determine the westward decay of the plume because of vertical mixing. An estimate of the relative importance of diffusion versus viscosity in the decay is the ratio of the first two terms in (3),

$$M_n \approx \frac{4R^2}{\pi^2 \sigma R_n^2}, \quad (4)$$

where $R_n = c_n/f = c_1/(nf)$ is the n th deformation radius, and R is the horizontal scale of the wind curl (appendix D), chosen here as the distance from zero to maximum wind stress (section 2).

According to (4), viscosity (diffusion) determines the decay when $M_n \ll 1$ ($M_n \gg 1$), that is, the forcing has a meridional scale R that is small (large) compared to the deformation radius R_n times $\pi\sqrt{\sigma}/2$ [which is ~ 5 when $\sigma = 10$, the value used in ROMS and a reasonable estimate for the real ocean—Pedlosky (1996)]. Note that M_n scales like n^2 so that, even if $M_1 \ll 1$, M_n will be much greater than 1 for n larger than a

TABLE 1. Relative importance of vertical diffusion vs vertical viscosity in the β -plume westward decay for the first baroclinic mode (M_1) and lowest baroclinic mode order for a dominant vertical diffusion (n_0), estimated for ROMS and OFES, and from 0.25° QuikSCAT observations. An estimated Prandtl number $\sigma \sim 10$ is used for OFES and the observations. See text for details.

Data	Lat (N)	R_1 (km)	R (km)	M_1	n_0
ROMS	30°	40	40	0.04	6
OFES-N	20°	60	200	0.45	2
OFES-Q	20°	60	100	0.11	4
Observed	20°	60	40	0.02	8

critical value n_0 . In the ROMS simulations, we estimate $M_1 \approx 0.04$ and $n_0 \approx 6$ (Table 1), which explains why the baroclinic flow is sensitive to both κ (Fig. 3c) and ν (Fig. 3d), but more so to the latter. In the OFES solutions, assuming an average value of $\sigma \sim 10$ (σ varies greatly with the KPP formulation), M_1 has larger values but still smaller than one, while n_0 is strictly larger than one (Table 1). Thus, while vertical diffusion likely plays a more important role in the OFES HLCC compared to the idealized simulations, vertical viscosity is still the dominant mixing process responsible for the HLCC westward deepening. On the other hand, the 1° QuikSCAT data used to force OFES (Sasaki et al. 2010) exhibit only one curl dipole near Hawaii (Fig. 8b), whereas 0.25° data have dipoles in the lee of each island (Chavanne et al. 2002; Yoshida et al. 2011). Using the same method, we estimate $M_1 \approx 0.02$ and $n_0 \approx 8$ (Table 1), so that the effect of viscosity likely dominates largely that of diffusion in the real HLCC, similar to the idealized simulations.

To estimate the zonal decay scale associated with each baroclinic mode when either viscosity or diffusion dominates, (3) can also be used. Specifically,

$$L_\nu = \frac{4BR^2c_1^2}{\pi^2\nu n^2 N^2} \quad \text{and} \quad L_\kappa = \frac{\beta c_1^4}{\kappa f^2 n^4 N^2} \quad (5)$$

are the e -folding zonal scales for viscosity and diffusion, respectively (appendix D). According to (5), the scales are smaller when mixing is enhanced (Figs. 3c,d), and they decrease with increasing n (preferential damping of higher-order modes). Furthermore, L_ν increases quadratically with the meridional scale of the forcing R , whereas L_κ does not vary with R .

This latter statement arises from the fact that the κ term in (3) is directly proportional to p_n , whereas the ν term involves the second meridional derivative of p_n . It is useful to go back to the vertical mode primitive equations (C9) to understand the origin of such different relationships to the meridional dimension (appendix C). The first meridional derivative of the ν term in the zonal momentum

equation (involving u_n) appears as a result of the computation of a vorticity equation from both momentum equations. The second meridional derivative of p_n is then obtained through the quasigeostrophic approximation. Hence, the ν term in the quasigeostrophic potential vorticity equation (3) represents the curl of viscosity, which is also the vertical gradient of the curl of the fluid turbulent stress. On the other hand, the computation of the vorticity equation also leads to the consideration of horizontal divergence, that is, vortex stretching, in the plume dynamics. For each vertical mode, vortex stretching is directly proportional to w_n as seen in the fourth line of (C8). The κ term in (3) then originates from the density equation relating p_n with w_n [fourth line of (C9)].

In other words, the κ term or vortex stretching directly acts on pressure perturbation and does not depend on the scale of the perturbation, that is, on the scale of the forcing. Conversely, the ν term or vertical gradient of the curl of the fluid turbulent stress acts on vorticity perturbation. This means that within the quasigeostrophic approximation, it acts on the horizontal derivatives of the gradient of pressure perturbation, and particularly on the second meridional derivative as a consequence of the anisotropy of the β plume. Thus, the ν term is enhanced (quadratically) for small meridional scales of the pressure perturbation, that is, for small meridional scales of the forcing.

To verify the relevance of these theoretical considerations to our idealized experiments, we obtained an additional simulation similar to the control run except with a forcing scale and amplitude of the wind twice as large ($R = 80$ km and $\tau_{\max} = 2.10^{-5}$ N m $^{-2}$), so that the curl amplitude is unchanged. Figure 3b confirms that, consistent with the above theory, baroclinic zonal scales are larger for larger forcing scales. In addition, the differences in the surface HLCC zonal extent in OFES-N and OFES-Q (Figs. 8c,d) also agree with theoretical predictions.

Note that the theoretical R^2 dependence in (5) suggests that, with $R = 40$ km in high-resolution scatterometer data (Chavanne et al. 2002; Yoshida et al. 2011), the zonal damping scale may be smaller in the real HLCC compared to OFES, and hence that the real HLCC deepening may be steeper than in the OFES simulations. Because the OFES-Q HLCC maximum at 1000 m is already directly below the surface maximum in the immediate lee of the islands (Fig. 6c), this questions the appropriateness of using the YoMaHa'07 signal 40° farther west (Figs. 7d and 11d) as the proxy for the HLCC deepening. As discussed previously, although not very likely, it is possible that the deep Argo signal in the far field does not represent the hypothesized westward deepening but some other dynamical feature. On

the other hand, such observation is qualitatively consistent with both OFES-N and ROMS and inconsistent only with OFES-Q. Perhaps there is something wrong with the HLCC in OFES-Q: as discussed in appendix B, OFES-Q does not reproduce the observed HLCC interannual variability well (Sasaki et al. 2010). One possible explanation is that OFES-Q might simulate SST fields that are inconsistent with the small-scale air–sea interaction over the real ocean and hence with the QuikSCAT wind forcing, leading to unrealistic behavior in the ocean circulation, a problem discussed by Chelton and Xie (2010, and references therein). Given the importance of air–sea feedbacks in the HLCC dynamics (Xie et al. 2001), and the fact that OFES-Q is the only model that implicitly accounts for such interaction in the present study, this hypothesis seems plausible. However, because the deep signal appears farther west in the observation compared to OFES-N (Fig. 5c), and because the larger forcing scale in the latter should produce the opposite effect according to the theoretical considerations presented here, it is also possible that the idealized model is too simplified to account for the complex dynamics of the real HLCC in the presence of finescale ocean–atmosphere coupling.

5. Summary and discussion

a. Summary

Experiments with an idealized primitive equation ocean model and an analytical LCS model suggest that the dynamical ocean response to small-scale wind forcing is sensitive to both vertical viscosity and vertical diffusion, which preferentially dampen baroclinic Rossby waves associated with higher-order vertical modes. As a result, the β plume induced by such compact forcing thickens, the surface jet weakens, and the strength of the deep flow increases with distance from the source. In contrast, the barotropic transport remains fairly uniform with longitude, in agreement with the Sverdrup dynamics. Consistent with the LCS theoretical model, resulting from a dynamically important vertical viscosity, zonal change in the flow vertical structure occurs over a shorter distance for smaller meridional scales of the forcing. A high-resolution OFES simulation forced by reanalyzed winds represents HLCC time-averaged baroclinic and barotropic structures similar to the idealized β plume. However, when forced by higher-resolution scatterometer winds, the OFES HLCC deep extension does not agree well with the idealized model, possibly because of the distributed forcing along the surface jet axis resulting from air–sea interaction, or because of nonlinear dynamics, eddy fluxes in particular. Nevertheless, the OFES simulations demonstrate the sensitivity of the

surface HLCC zonal extent to the wind stress curl forcing scale, as predicted by theory. Whereas our theoretical results are not expected to be quantitatively robust, they are qualitatively useful in that they can help compare numerical solutions with different mixing schemes. Although the LCS, ROMS, and OFES models use stratification-dependent, constant, and KPP-derived mixing coefficients, respectively, they exhibit qualitatively similar baroclinic ocean responses to localized forcing and similar sensitivities to the scale of this forcing. On the other hand, the westward decay of the HLCC transport is likely due to the wind stress curl in the far field, though nonlinear stress may also play a role. This decay likely contributes to the surface flow decay, in addition to the effect of the vertical mixing mechanism. The OFES solutions reveal the existence of a deep HLCC extension, which is also found in Argo float trajectory data, although with different characteristics and large uncertainties that do not allow making any firm conclusions. Still, this qualitative agreement supports the relevance of the baroclinic β -plume dynamics to the real ocean and provides new insight into the HLCC mean structure.

b. Impact of background currents

Whereas the circulation of the World Ocean is characterized by a system of large-scale gyres, effects of the background flow are neglected in the idealized experiments. As discussed in section 3b(1), in the case of the Hawaiian Islands, the NEC acts to cancel out the eastward HLCC to the west of the date line; moreover, the surface and subsurface branches of the HLCC also appear separated because of the superimposition of the NEC, which has a different vertical structure. It is known that mean flow can affect the propagation characteristics of Rossby waves and eddies (Luyten et al. 1983; Rhines and Young 1982; Chang and Philander 1989), and therefore affect the westward extension of β plumes. Depending on the strength and direction of the flow, different dynamical effects may be anticipated. A large-scale westward zonal flow such as the NEC, superimposed on the double-gyre response to a curl dipole such as the HLCC, may enhance the westward-flowing jets while having a weak effect on the eastward-flowing jet, which is protected by the island topographic barrier (Liu et al. 2003). The resulting increased meridional shear may then enhance baroclinic and barotropic instabilities and the associated generation of mesoscale eddies (e.g., Yu et al. 2003; Yoshida et al. 2010), which may affect the mean HLCC horizontal and vertical structures because eddies may either draw energy from the mean flow through dissipation (Yu et al. 2003) or reinforce the mean jet through Reynolds shear stress (Lumpkin and Flament

2013). Under certain conditions, the background flow may also be able to advect eddies shed around the islands and accelerate their westward drift (Holland and Mitchum 2001), with potential implications for the plume structure. However, the fact that the HLCC, once isolated from the gyre flow in which it is embedded, compares favorably to the idealized model without background flow is an indication that any interaction between the gyre flow and the HLCC β plume may be weak.

On the other hand, large-scale meridional flow may have different effects. The intrinsic baroclinic instability of meridional flows (Walker and Pedlosky 2002) is a source of nonlinearity that may have an impact on the β plume. In addition, meridional advection of slow Rossby waves and eddies is expected even for weak flow regimes (Luyten et al. 1983; Rhines and Young 1982). Such advection may contribute to the westward HLCC deepening by shifting higher-order baroclinic Rossby waves southward (Qiu and Durland 2002). However, the damping of higher-order baroclinic Rossby waves by vertical mixing is unlikely to be modified by these dynamics: vertical mixing may still be able to damp Rossby waves, whether shifted southward or not.

c. Impact of the island mass

In this study, the effect of the island mass on the generation of β plumes has been neglected. It is however clear that tall, deep water islands such as the Hawaiian Islands act as topographic barriers to both the oceanic and atmospheric flows, thus potentially generating localized vorticity in the ocean through both wind and topographic forcings.

The effects of the island mass were studied by Qiu and Durland (2002). They used a 2½-layer model in both idealized and realistic configurations to show that the presence of the island mass within the subtropical gyre generates barotropic zonal jets to the west that contribute significantly to the HLCC barotropic transport by reducing it on its southern flank and enhancing it on its northern flank, with an overall 20% reduction in the net transport. The authors do, however, acknowledge that it may not be the primary forcing of the HLCC. Modeling results obtained with ROMS forced by smooth wind fields have suggested that barotropic zonal jets may also be generated in the lee of tall islands of the southwest Pacific as a result of topographic forcing (Couvelard et al. 2008).

The relative importance of the two effects and how they interact is an interesting future study. It has indeed been a subject of controversy in the recent literature. Jiménez et al. (2008) studied the relative importance of these two forcings on eddy shedding by a tall, deep water island in an idealized ocean model on the f plane (thus

not capable of representing β -plume dynamics) applied to the island of Gran Canaria. They found that topographic forcing was a necessary condition for the generation of a von Kármán vortex street in the island lee, and that wind forcing was only required in the case of weak background oceanic flow. Kersalé et al. (2011) performed sensitivity experiments with a realistic configuration of the ROMS model for the Hawaiian Islands to infer the relative importance of these two forcings on the generation of mesoscale eddies in the lee of the islands and found qualitatively consistent results with Jiménez et al. (2008). However, Jia et al. (2011) used a similar approach based on the use of the Hybrid Coordinate Ocean Model (HYCOM; Bleck 2002) and found opposite results, with a largely dominant role of wind forcing. In agreement with these results, Yoshida et al. (2010) found a close relationship between 60-day Hawaiian lee eddies and high-frequency wind forcing based on satellite data. Interestingly, they also found that 100-day eddy signals that dominate the HLCC region farther west (near 165°W) were more likely the result of barotropic instability of the sheared NEC and HLCC.

Although these previous works focused on eddy shedding rather than β -plume or HLCC generation, the two questions are related. Indeed, the HLCC is the long-term mean manifestation of westward-propagating mesoscale eddies of both signs, anticyclonic to the south and cyclonic to the north (e.g., Holland and Mitchum 2001; Calil et al. 2008). In addition, eddies in both the island lee and the remote region may act as additional sources and sinks of vorticity that can have a significant influence on the time-mean zonal jet as discussed in the previous section.

d. Striations

The recent detection of ubiquitous stationary quasi-zonal jet-like structures (striations) in the World Ocean (Maximenko et al. 2005, 2008) may indicate that β plumes survive in most large-scale flows. Indeed, β plumes have been suggested as a mechanism for the formation of some striations (Centurioni et al. 2008; Hristova et al. 2008; Melnichenko et al. 2010; Wang et al. 2012). In particular, striations have been found in both zonal and meridional gyre flows. In subtropical eastern boundary current regions, they are tilted toward the equator, consistently with the equatorward flow (Maximenko et al. 2008; Melnichenko et al. 2010). Interestingly enough, the HLCC contributes to the global grid of striations, as suggested by Fig. 1a in Maximenko et al. (2008).

e. Need for more observations

This study emphasizes the need for high-resolution winds to force ocean models. It also calls for more

accurate rates of ocean mixing. For a given forcing, the spatial scales of the β -plume vertical spreading depend on the details of vertical mixing, which in numerical models rely on imperfect parameterizations of subgrid-scale turbulent processes. Likewise, criterion M_n , which depends on the forcing horizontal scale, also depends on the parameterized mixing scheme. In fact, the intensity of eddy-induced vertical mixing may be sensitive to characteristics of the wind forcing, such as high-frequency spectrum as suggested by Cardona and Bracco (2012), and possibly spatial structure as well. Differences in vertical HLCC structure and surface decay between the two OFES solutions may then be partly caused by enhanced eddy mixing in the OFES-Q run associated with the smaller-scale QuikSCAT wind-curl dipole. A better knowledge of vertical mixing, which is a main challenge of modern oceanography, is needed for a better modeling of the westward deepening of the HLCC and other wind-driven β plumes.

Acknowledgments. We are grateful to F. Ascani, B. Qiu, H. Sasaki, S.-P. Xie, and Z. Yu for fruitful discussions. We also wish to thank two anonymous reviewers for helpful comments on an earlier version of this paper. The ROMS simulations were performed on Jaws, a PC cluster at HOSC. The OFES simulations were conducted on the Earth Simulator of the Japan Agency for Marine-Earth Science and Technology (JAMSTEC), and the outputs were accessed via the APDRC, which also provided access to YoMaHa'07 data. This research was partly supported by the JAMSTEC, by NASA through Grant NNX07AG53G, and by NOAA through Grant NA17RJ1230, which sponsor research at the International Pacific Research Center (IPRC). Additional support was provided by NOAA through Collaborative Agreements NA09OAR4320075 and NA08OAR4320910, which sponsor research at the Joint Institute for Marine and Atmospheric Research (JIMAR), and by the NASA Grants NNX08AR49G and NNX10AE97G.

APPENDIX A

Analytical Expression of the Barotropic Flow

To construct the wind stress vortex that forces the idealized model, we introduce the Gaussian streamfunction

$$\psi_a = R\tau_{\max}\sqrt{e}\exp\left(-\frac{x^2 + y^2}{2R^2}\right). \quad (\text{A1})$$

The expression for the resulting wind stress vector $\boldsymbol{\tau}$ is then

$$\boldsymbol{\tau} = \mathbf{k} \times \nabla\psi_a, \quad (\text{A2})$$

where \mathbf{k} is a unit vector pointing upward. It follows that τ_{\max} is the maximum wind stress, and it occurs at a distance R from the vortex center. The vertical component of wind stress curl (referred in the rest of the paper simply as wind stress curl) is then

$$\mathbf{k} \cdot \nabla \times \boldsymbol{\tau} = \frac{\tau_{\max}\sqrt{e}}{R} \left(\frac{x^2 + y^2}{R^2} - 2 \right) \exp\left(-\frac{x^2 + y^2}{2R^2}\right). \quad (\text{A3})$$

The meridional barotropic oceanic flow $V = \partial\Psi/\partial x$ is given by Sverdrup balance (1), where Ψ is the barotropic streamfunction.

The zonal barotropic flow U is finally obtained from the depth-integrated continuity equation by integrating the meridional shear of the meridional barotropic flow zonally from the basin eastern boundary, yielding

$$U = \int_x^{x_e} \frac{\partial V}{\partial y} dx, \quad (\text{A4})$$

where x_e is the eastward distance between the vortex center and the eastern boundary. Substituting V into (A4) and using (A3) gives

$$U = \frac{\tau_{\max}\sqrt{e}}{\beta\rho_b R^4} y e^{-y^2/2R^2} \left\{ \sqrt{\frac{\pi}{2}} (3R^2 - y^2) \left[\operatorname{erf}\left(\frac{x_e}{\sqrt{2}R}\right) - \operatorname{erf}\left(\frac{x}{\sqrt{2}R}\right) \right] - R \left(x e^{-x^2/2R^2} - x_e e^{-x_e^2/2R^2} \right) \right\}, \quad (\text{A5})$$

where β is the meridional gradient of the Coriolis parameter, ρ_b is the average density of the water column in the study region, and

$$\operatorname{erf}(x) = \frac{2}{\sqrt{\pi}} \int_0^x e^{-t^2} dt \quad (\text{A6})$$

is the error function.

APPENDIX B

Errors Associated with the YoMaHa'07 Velocity Estimates

The YoMaHa'07 dataset contains both station data, where a surface and a deep velocity estimate were derived for each Argo float cycle with corresponding geographical coordinates and time, and the gridded bin-averaged data used in this study, where only mean values, standard deviation, and sample size are available. Thus, when using the gridded data only standard errors may be explicitly quantified (see below). However, for station data, error estimates in the individual Argo velocity estimates are provided (Lebedev et al. 2007).

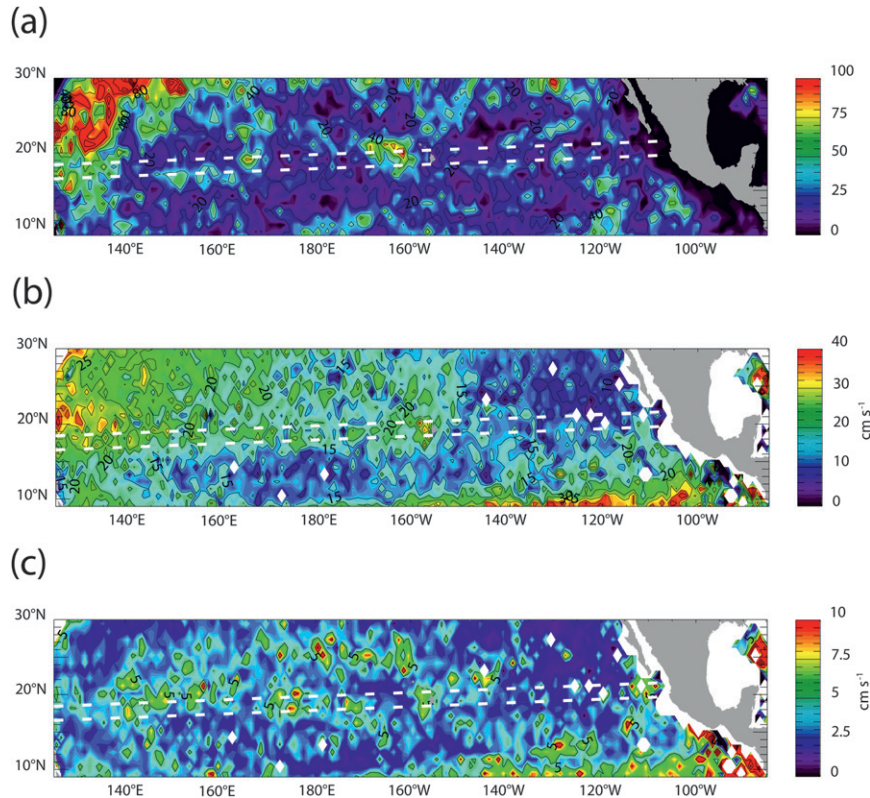


FIG. B1. (a) Data density (number of observations per $1^\circ \times 1^\circ$ bin), (b) zonal current std dev, and (c) standard error of the mean zonal current in the Argo float trajectory data (YoMaHa'07) at sea surface over 1997–2007. The error is computed as the std dev divided by the square root of the number of observations. Units are cm s^{-1} in (b),(c). CI is 20 in (a) and 5 cm s^{-1} in (b),(c). The thick dashed lines on all panels are the same as in Fig. 7. The relatively large error in HLCC mean surface velocities away from the island lee results from both scarce data density and strong variability. Note that this error estimate does not account for errors in the individual Argo velocity estimates.

The error associated with surface velocity estimates does not include the float slip relative to surrounding water under the joint force of wind and waves. It was estimated with drogued surface drifters (Niiler et al. 1995) to be of the order of a few centimeters per second under moderate winds, which characterize the trade wind region to the west of the Hawaiian Islands. The slip may be stronger for the undrogued Argo floats. The error associated with deep velocity estimates does not account for the real baroclinic velocity structure and does not include variations because of inertial oscillations, among other uncertainties. For more details on the calculation of the surface and deep velocity estimates and associated errors, the reader is invited to refer to Lebedev et al. (2007). With these limitations in mind, it is worth noting that, according to Lebedev et al. (2007), both surface and deep velocities are an order of magnitude higher than their respective errors on the global scale. Unfortunately, the authors

do not provide the geographical distribution of error estimates.

Temporal sampling is another source of uncertainty. Although the YoMaHa'07 dataset covers the 11-yr period from 1997 to 2007, the HLCC axis has been sampled without any major spatial gaps only for the 3-yr period from 2005 to 2007 (Lebedev et al. 2007; their Fig. 6), so the ensemble mean velocities may not be representative of the “true” decadal means. To address questions such as whether the measurements are evenly spaced in time, or whether they are clustered in different time periods at different locations of the HLCC axis, requires a complete analysis of individual Argo float data, which is beyond the scope of the present study.

This limits significantly the comparison of the observed ensemble means with the decadal mean simulated by OFES over 1999–2008 [see section 3b(2)]. According to altimeter data, 2005 was a year of enhanced HLCC velocity to the east of 170°E , while 2006 and 2007 had

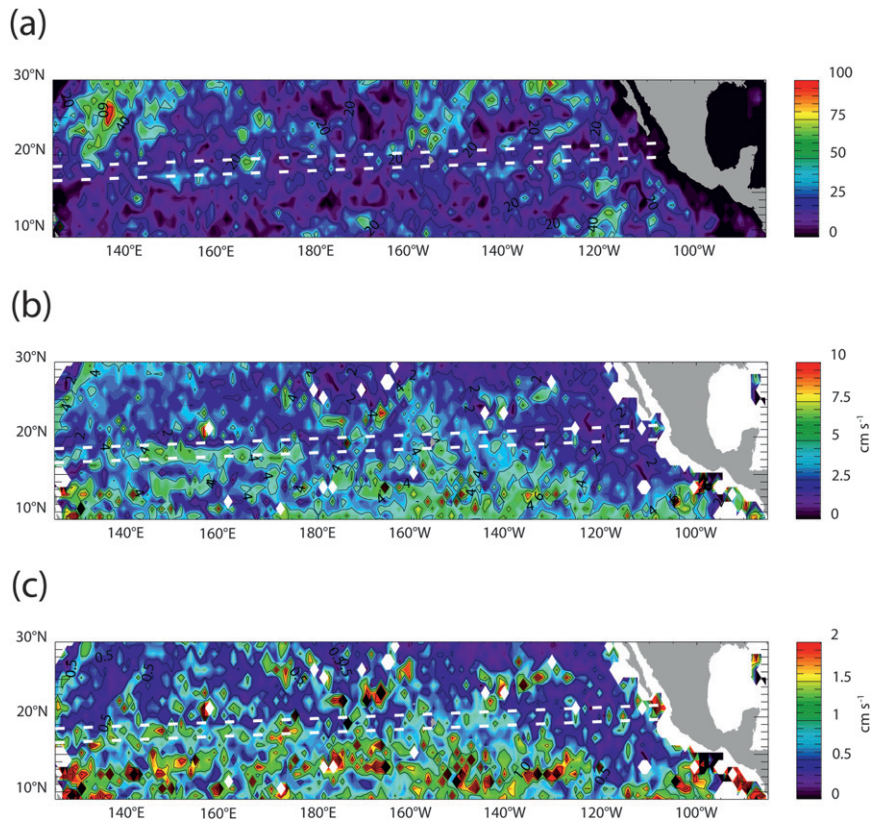


FIG. B2. As in Fig. B1, but for 1000-m depth. Note the changes in color bars. CI is 20 in (a), 2 cm s^{-1} in (b), and 0.5 cm s^{-1} in (c). Large error in HLCC mean deep velocities results from scarce data density and strong variability. In contrast to the surface, the latter is highest in the tropics and exhibits a possible deep HLCC extension already seen in the mean. Note that this error estimate does not account for errors in the individual Argo velocity estimates.

HLCC velocity closer to the average over 1993–2007 (Sasaki et al. 2010). On the other hand, the 2005 anomaly is not reproduced in OFES-Q and the model HLCC velocities tend to be weaker than observed over 2000–07 (Sasaki et al. 2010). This suggests that the YoMaHa'07 ensemble means (OFES-Q decadal means) may overestimate (underestimate) the true decadal means. Unfortunately, the associated uncertainty is hard to quantify, particularly for deep velocities, for which no other observations are available. Therefore, the zonal dependence of surface and deep mean velocities along the HLCC axis in YoMaHa'07 and OFES-Q may only be compared qualitatively and one needs to be cautious even with qualitative comparisons given all the uncertainties of the YoMaHa'07 data.

It should also be kept in mind that the YoMaHa'07 velocities are obtained by averaging a scarce ensemble of in situ data in a region of strong mesoscale eddy activity (e.g., Calil et al. 2008), so the associated uncertainty is large. The standard error associated with the HLCC surface current estimate (Fig. B1c), comparable with the

mean value (Fig. 7c), is a result of both scarce data density along the HLCC axis (~ 20 observations per $1^\circ \times 1^\circ$ grid box over the 11-yr period; Fig. B1a) and elevated surface current variability (Fig. B1b), typically $15\text{--}20 \text{ cm s}^{-1}$. The error along the HLCC axis is typically $3\text{--}5 \text{ cm s}^{-1}$ (Fig. B1c), except between 170° and 160°W , where higher data density (Fig. B1a) allows for a smaller $2\text{--}3 \text{ cm s}^{-1}$ error. In the immediate lee of the island, where the HLCC strength reaches 25 cm s^{-1} (Fig. 7c), errors remain relatively small.

At 1000 m, the data density pattern is similar to the surface but with fewer observations (Fig. B2a), because many Argo floats are programmed for a different parking depth (Lebedev et al. 2007). The error in deep velocities (typically 1 cm s^{-1} ; Fig. B2c) is large compared to the $2\text{--}3 \text{ cm s}^{-1}$ mean deep currents along the HLCC axis to the west of 165°E (Fig. 7d). Interestingly, the large-scale variability pattern is very different from that at the surface (Fig. B1b), with larger values in the tropics compared to the subtropics and a clear banded structure to the south of $\sim 20^\circ\text{N}$ (Fig. B2b) also seen in the mean

(Fig. 7d). This is reminiscent of the alternating deep equatorial zonal jets recently found by Ascani et al. (2010) and by Cravatte et al. (2012) through similar treatments of Argo float trajectories. Noteworthy, the deep tropical jets are also evident in OFES-Q outputs (Fig. 7b). This contrast between surface/subsurface flow patterns may result from the strong signal of the surface-intensified subtropical gyre, which is weak below the thermocline (Figs. 5 and 6).

APPENDIX C

Quasigeostrophic Potential Vorticity Equation for the n th Vertical Mode

Following McCreary (1981), the steady-state hydrostatic linearized primitive equations are

$$\left. \begin{aligned} -fv + \frac{p_x}{\rho_b} &= (\nu u_z)_z, \\ fu + \frac{p_y}{\rho_b} &= (\nu v_z)_z, \\ p_z &= -\rho g, \\ -\frac{\rho_b N^2 w}{g} &= (\kappa \rho)_{zz}, \quad \text{and} \\ u_x + v_y + w_z &= 0, \end{aligned} \right\} \quad (C1)$$

where u, v , and w are the zonal, meridional, and vertical velocity anomalies, respectively, p and ρ are the pressure and density anomalies, g is the acceleration due to gravity, ρ_b is the average density of the water column in the study region, and subscripts x, y , and z indicate a partial derivative with respect to x, y , and z , respectively.

The LCS model considers the following rigid-lid surface boundary conditions at $z = 0$

$$\nu u_z = \frac{\tau^x}{\rho_b}, \quad \nu v_z = \frac{\tau^y}{\rho_b}, \quad w = 0, \quad \text{and} \quad \rho = 0, \quad (C2)$$

and flat-bottom boundary conditions at $z = -D$

$$\nu u_z = \nu v_z = w = \rho = 0, \quad (C3)$$

where τ^x and τ^y are the zonal and meridional surface wind stress components, respectively. These are standard boundary conditions, except the assumption of constant background density, which implies that the atmosphere and the ocean floor act as constant-temperature heat sources. Whereas the bottom boundary condition generally does not affect the baroclinic flow, which is mostly confined in the upper ocean, the surface boundary

condition means that the LCS does not consider any SST anomaly, which limits to some extent the application of the LCS theory to the real ocean. Both restrictions, however, are necessary for the expansion in vertical modes.

Rewriting (C1) with the formulation for mixing coefficients (2) yields

$$\left. \begin{aligned} -fv + \frac{p_x}{\rho_b} &= AF(u), \\ fu + \frac{p_y}{\rho_b} &= AF(v), \\ u_x + v_y &= -\frac{A}{\sigma \rho_b} F[F(p)], \\ w &= \frac{1}{N^2 \sigma \rho_b} [F(p)]_z, \quad \text{and} \\ \rho &= -\frac{p_z}{g}, \end{aligned} \right\} \quad (C4)$$

where $F(q) = (q_z/N^2)_z$, and q is u, v , or p .

Solutions to (C4) can be expressed in terms of eigenfunctions $\psi_n(z)$ of

$$F[\psi_n(z)] = -\frac{\psi_n(z)}{c_n^2}, \quad (C5)$$

subject to the boundary conditions that

$$\psi_{nz} = 0 \quad \text{at} \quad z = 0 \quad \text{and} \quad z = -D, \quad (C6)$$

where c_n is the phase speed of the n th mode gravity wave. A convenient normalization for the eigenfunctions is

$$\psi_n(0) = 1. \quad (C7)$$

The eigenfunctions are the barotropic ($n = 0$) and baroclinic ($n \geq 1$) vertical normal modes of the system.

Solutions can be represented as expansions in the eigenfunctions as follows

$$\left. \begin{aligned} u(x, y, z, t) &= \sum_{n=0}^{+\infty} u_n(x, y, t) \psi_n(z), \\ v(x, y, z, t) &= \sum_{n=0}^{+\infty} v_n(x, y, t) \psi_n(z), \\ p(x, y, z, t) &= \sum_{n=0}^{+\infty} p_n(x, y, t) \psi_n(z), \\ w(x, y, z, t) &= \sum_{n=0}^{+\infty} w_n(x, y, t) \int_{-D}^z \psi_n(z) dz, \quad \text{and} \\ \rho(x, y, z, t) &= \sum_{n=0}^{+\infty} \rho_n(x, y, t) \psi_{nz}(z), \end{aligned} \right\} \quad (C8)$$

where u_n, v_n, w_n, p_n , and ρ_n are the expansion coefficients for zonal, meridional, and vertical velocity components, pressure, and density. Spatial and temporal dependences are omitted hereafter for clarity.

Equations governing the expansion coefficients are found by first substituting u, v, w, p , and ρ in (C4) by their expressions in (C8). Then, each resulting equation is multiplied by ψ_n and integrated over the water column. Noting that ψ_n form an orthogonal set, the right-hand sides are integrated twice by parts. Using boundary conditions (C2), (C3), and (C6), normalization (C7), and (C5) gives steady-state equations for the expansion coefficients,

$$\left. \begin{aligned} -fv_n + \frac{p_{nx}}{\rho_b} + \frac{\nu N^2}{c_n^2} u_n &= F_n, \\ fu_n + \frac{p_{ny}}{\rho_b} + \frac{\nu N^2}{c_n^2} v_n &= G_n, \\ u_{nx} + v_{ny} + \frac{\kappa N^2}{\rho_b c_n^4} p_n &= 0, \\ w_n &= -\frac{\kappa N^2}{\rho_b c_n^4} p_n, \quad \text{and} \\ \rho_n &= -\frac{p_n}{g}, \end{aligned} \right\} \quad (\text{C9})$$

where

$$\left. \begin{aligned} F_n &= \frac{\tau^x}{\rho_b \int_{-D}^0 \psi_n^2 dz} \quad \text{and} \\ G_n &= \frac{\tau^y}{\rho_b \int_{-D}^0 \psi_n^2 dz} \end{aligned} \right\} \quad (\text{C10})$$

describe how the wind forcing couples to each mode.

To derive a single equation for p_n , we first subtract the y derivative of the first line of (C9) from the x derivative of the second to get

$$f(u_{nx} + v_{ny}) + \beta v_n + \frac{\nu N^2}{c_n^2} (v_{nx} - u_{ny}) = G_{nx} - F_{ny}. \quad (\text{C11})$$

We then assume that u_n and v_n are in geostrophic balance in the far field (quasigeostrophic approximation)

$$\left. \begin{aligned} f_0 v_n &\approx \frac{p_{nx}}{\rho_b} \quad \text{and} \\ f_0 u_n &\approx -\frac{p_{ny}}{\rho_b} \end{aligned} \right\}, \quad (\text{C12})$$

where $f = f_0$ in the quasigeostrophic limit. Substituting (C12) into (C11) and using the third line of (C9) gives (3), the steady-state response for p_n . This is the β -plume quasigeostrophic potential vorticity balance for each vertical normal mode. It simplifies to (1) for the barotropic mode ($n = 0$), for which $c_0 \rightarrow \infty$, $\psi_0(z) = 1$, $F_0 = \tau^x/(\rho_b D)$, and $G_0 = \tau^y/(\rho_b D)$.

APPENDIX D

Scaling Arguments for Viscosity and Diffusion

Because the zonal scale of a β plume is large compared to its meridional scale, (3) may be approximated by

$$\frac{N^2}{c_n^2} \left(\nu p_{nyy} - \frac{\kappa}{R_n^2} p_n \right) + \beta p_{nx} = \rho_b f (G_{nx} - F_{ny}), \quad (\text{D1})$$

where $R_n = c_n/f = c_1/(nf)$ is the n th deformation radius. Approximating the meridional structure of the plume by a sine function with a wavelength of $4R$ (Fig. 2a), where R is the distance from zero to maximum wind stress (Fig. 1), gives

$$p_{nyy} \approx -\frac{\pi^2}{4R^2} p_n, \quad (\text{D2})$$

and the ratio of the κ term over the ν term on the left-hand side of (D1) [or (3)] is then given by (4). Viscosity (diffusion) dominates in (3) when $M_n \ll 1$ ($M_n \gg 1$).

To estimate the e -folding zonal scale L_n associated with each baroclinic mode when either viscosity or diffusion dominates, (3) may also be used. Noting that the zonal plume structure may be approximated by an exponential decay (Fig. 2c)

$$p_{nx} \approx -\frac{p_n}{L_n} \quad (\text{D3})$$

balancing the β term in (D1) with either the viscous or diffusive term [first two terms on the left-hand side of (D1)] and using (D2) and (D3) gives (5).

REFERENCES

- Antonov, J. I., and Coauthors, 2010: *Salinity*. Vol. 2, *World Ocean Atlas 2009*, NOAA Atlas NESDIS 69, 184 pp.
- Aoki, Y., T. Suga, and K. Hanawa, 2002: Subsurface subtropical fronts of the North Pacific as inherent boundaries in the ventilated thermocline. *J. Phys. Oceanogr.*, **32**, 2299–2311.
- Ascani, F., E. Firing, P. Dutrieux, J. P. McCreary, and A. Ishida, 2010: Deep equatorial ocean circulation induced by a forced-dissipated Yanai beam. *J. Phys. Oceanogr.*, **40**, 1118–1142.
- Bleck, R., 2002: An oceanic general circulation model framed in hybrid isopycnic-Cartesian coordinates. *Ocean Modell.*, **4**, 55–88, doi:10.1016/S1463-5003(01)00012-9.

- Calil, P. H. R., K. J. Richards, Y. Jia, and R. Bidigare, 2008: Eddy activity in the lee of the Hawaiian Islands. *Deep-Sea Res.*, **55**, 1179–1194, doi:10.1016/j.dsr2.2008.01.008.
- Cardona, Y., and A. Bracco, 2012: Enhanced vertical mixing within mesoscale eddies due to high frequency winds in the South China Sea. *Ocean Modell.*, **42**, 1–15, doi:10.1016/j.ocemod.2011.11.004.
- Centurioni, L. R., J. C. Ohlmann, and P. P. Niiler, 2008: Permanent meanders in the California Current System. *J. Phys. Oceanogr.*, **38**, 1690–1710.
- Chang, P., and S. G. H. Philander, 1989: Rossby wave packets in baroclinic mean currents. *Deep-Sea Res.*, **36**, 17–37, doi:10.1016/0198-0149(89)90016-2.
- Chavanne, C., P. Flament, R. Lumpkin, B. Dousset, and A. Bentamy, 2002: Scatterometer observations of wind variations induced by oceanic islands: Implications for wind-driven ocean circulation. *Can. J. Remote Sens.*, **28**, 466–474.
- Chelton, D. B., and S.-P. Xie, 2010: Coupled ocean–atmosphere interaction at oceanic mesoscales. *Oceanography*, **23**, 52–69, doi:10.5670/oceanog.2010.05.
- , R. A. deSzoeke, M. G. Schlax, K. El Naggar, and N. Siwertz, 1998: Geographical variability of the first baroclinic Rossby radius of deformation. *J. Phys. Oceanogr.*, **28**, 433–460.
- , M. G. Schlax, M. H. Freilich, and R. F. Milliff, 2004: Satellite measurements reveal persistent small-scale features in ocean winds. *Science*, **303**, 978–983, doi:10.1126/science.1091901.
- Cornillon, P., and K.-A. Park, 2001: Warm core ring velocities inferred from NSCAT. *Geophys. Res. Lett.*, **28**, 575–578.
- Couvelard, X., P. Marchesiello, L. Gourdeau, and J. Lefèvre, 2008: Barotropic zonal jets induced by islands in the southwest Pacific. *J. Phys. Oceanogr.*, **38**, 2185–2204.
- Cravatte, S., W. S. Kessler, and F. Marin, 2012: Intermediate zonal jets in the tropical Pacific Ocean observed by Argo floats. *J. Phys. Oceanogr.*, **42**, 1475–1485.
- Davey, M. K., and P. D. Killworth, 1989: Flows produced by discrete sources of buoyancy. *J. Phys. Oceanogr.*, **19**, 1279–1290.
- Haidvogel, D. B., and P. B. Rhines, 1983: Waves and circulation driven by oscillatory winds in an idealized ocean basin. *Geophys. Astrophys. Fluid Dyn.*, **25**, 1–63.
- , and Coauthors, 2008: Ocean forecasting in terrain-following coordinates: Formulation and skill assessment of the Regional Ocean Modeling System. *J. Comput. Phys.*, **227**, 3595–3624.
- Holland, C. L., and G. T. Mitchum, 2001: Propagation of Big Island eddies. *J. Geophys. Res.*, **106** (C1), 935–944.
- Hristova, H. G., J. Pedlosky, and M. A. Spall, 2008: Radiating instability of a meridional boundary current. *J. Phys. Oceanogr.*, **38**, 2294–2307.
- Jia, Y., and Coauthors, 2011: Generation of mesoscale eddies in the lee of the Hawaiian Islands. *J. Geophys. Res.*, **116**, C11009, doi:10.1029/2011JC007305.
- Jiménez, B., P. Sangrà, and E. Mason, 2008: A numerical study of the relative importance of wind and topographic forcing on oceanic eddy shedding by tall, deep water islands. *Ocean Modell.*, **22**, 146–157, doi:10.1016/j.ocemod.2008.02.004.
- Kalnay, E., and Coauthors, 1996: The NCEP/NCAR 40-Year Reanalysis Project. *Bull. Amer. Meteor. Soc.*, **77**, 437–471.
- Kelly, K. A., S. Dickinson, M. J. McPhaden, and G. C. Johnson, 2001: Ocean currents evident in satellite wind data. *Geophys. Res. Lett.*, **28**, 2469–2472.
- Kersalé, M., A. M. Doglioli, and A. A. Petrenko, 2011: Sensitivity study of the generation of mesoscale eddies in a numerical model of Hawaii islands. *Ocean Sci.*, **7**, 277–291, doi:10.5194/os-7-277-2011.
- Kessler, W. S., G. C. Johnson, and D. W. Moore, 2003: Sverdrup and nonlinear dynamics of the Pacific equatorial currents. *J. Phys. Oceanogr.*, **33**, 994–1008.
- Kida, S., J. F. Price, and J. Yang, 2008: The upper-oceanic response to overflows: A mechanism for the Azores Current. *J. Phys. Oceanogr.*, **38**, 880–895.
- , J. Yang, and J. F. Price, 2009: Marginal sea overflows and the upper ocean interaction. *J. Phys. Oceanogr.*, **39**, 387–403.
- Kobashi, F., and H. Kawamura, 2002: Seasonal variation and instability nature of the North Pacific Subtropical Countercurrent and the Hawaiian Lee Countercurrent. *J. Geophys. Res.*, **107**, 3185, doi:10.1029/2001JC001225.
- Large, W., J. C. McWilliams, and S. Doney, 1994: Oceanic vertical mixing: A review and a model with a nonlocal boundary layer parameterization. *Rev. Geophys.*, **32**, 363–403.
- Lebedev, K., H. Yoshinari, N. A. Maximenko, and P. W. Hacker, 2007: YoMaHa'07: Velocity data assessed from trajectories of Argo floats at parking level and at the sea surface. IPRC Tech. Note 4(2), 16 pp. [Available online at <http://apdrc.soest.hawaii.edu/projects/yomaha/>.]
- Liu, Q., S. Wang, Q. Wang, and W. Wang, 2003: On the formation of Subtropical Countercurrent to the west of the Hawaiian Islands. *J. Geophys. Res.*, **108**, 3167, doi:10.1029/2002JC001366.
- Locarnini, R. A., A. V. Mishonov, J. I. Antonov, T. P. Boyer, H. E. Garcia, O. K. Baranova, M. M. Zweng, and D. R. Johnson, 2010: *Temperature*. Vol. 1, *World Ocean Atlas 2009*, NOAA Atlas NESDIS 68, 184 pp.
- Lumpkin, R., and P. J. Flament, 2013: Extent and energetics of the Hawaiian Lee Countercurrent. *Oceanography*, **26**, 58–65, doi:10.5670/oceanog.2013.05.
- Luyten, J. R., J. Pedlosky, and H. Stommel, 1983: The ventilated thermocline. *J. Phys. Oceanogr.*, **13**, 292–309.
- Masumoto, Y., and Coauthors, 2004: A fifty-year eddy-resolving simulation of the world ocean—Preliminary outcomes of OFES (OGCM for the Earth Simulator). *J. Earth Simul.*, **1**, 35–56.
- Maximenko, N. A., B. Bang, and H. Sasaki, 2005: Observational evidence of alternating zonal jets in the world ocean. *Geophys. Res. Lett.*, **32**, L12607, doi:10.1029/2005GL022728.
- , O. V. Melnichenko, P. P. Niiler, and H. Sasaki, 2008: Stationary mesoscale jet-like features in the ocean. *Geophys. Res. Lett.*, **35**, L08603, doi:10.1029/2008GL033267.
- McCreary, J. P., 1981: A linear stratified ocean model of the Equatorial Undercurrent. *Philos. Trans. Roy. Soc. London*, **A298**, 603–635.
- , and Coauthors, 2007: Interactions between the Indonesian throughflow and circulations in the Indian and Pacific Oceans. *Prog. Oceanogr.*, **75**, 70–114.
- Melnichenko, O. V., N. A. Maximenko, N. Schneider, and H. Sasaki, 2010: Quasi-stationary striations in basin-scale oceanic circulation: Vorticity balance from observations and eddy-resolving model. *Ocean Dyn.*, **60**, 653–666.
- Niiler, P. P., A. S. Sybrandy, K. Bi, P. M. Poulain, and D. Bitterman, 1995: Measurements of water-following characteristics of Tristar and Holey-sock drifters. *Deep-Sea Res.*, **42**, 1951–1964.
- Özgökmen, T. M., E. P. Chassignet, and C. G. H. Rooth, 2001: On the connection between the Mediterranean outflow and the Azores Current. *J. Phys. Oceanogr.*, **31**, 461–480.
- Pedlosky, J., 1996: *Ocean Circulation Theory*. Springer-Verlag, Berlin, 453 pp.

- Qiu, B., and T. S. Durland, 2002: Interaction between an island and the ventilated thermocline: Implications for the Hawaiian Lee Countercurrent. *J. Phys. Oceanogr.*, **32**, 3408–3426.
- , D. A. Koh, C. Lumpkin, and P. Flament, 1997: Existence and formation mechanism of the North Hawaiian Ridge Current. *J. Phys. Oceanogr.*, **27**, 431–444.
- Rhines, P. B., 1994: Jets. *Chaos*, **4**, 313–339.
- , and W. R. Young, 1982: A theory of wind-driven circulation. I. Mid-ocean gyres. *J. Mar. Res.*, **40**, 559–596.
- Sasaki, H., and M. Nonaka, 2006: Far-reaching Hawaiian Lee Countercurrent driven by wind-stress curl induced by warm SST band along the current. *Geophys. Res. Lett.*, **33**, L13602, doi:10.1029/2006GL026540.
- , S.-P. Xie, B. Taguchi, M. Nonaka, and Y. Masumoto, 2010: Seasonal variations of the Hawaiian Lee Countercurrent induced by the meridional migration of the trade winds. *Ocean Dyn.*, **60**, 705–715, doi:10.1007/s10236-009-0258-6.
- Shchepetkin, A. F., and J. C. McWilliams, 2005: The Regional Oceanic Modeling System: A split-explicit, free-surface, topography-following-coordinate ocean model. *Ocean Modell.*, **9**, 347–404.
- Small, R. J., and Coauthors, 2008: Air–sea interaction over ocean fronts and eddies. *Dyn. Atmos. Oceans*, **45**, 274–319.
- Spall, M. A., 2000: Buoyancy-forced circulations around islands and ridges. *J. Mar. Res.*, **58**, 957–982.
- Stommel, H. M., 1982: Is the South Pacific helium-3 plume dynamically active? *Earth Planet. Sci. Lett.*, **61**, 63–67.
- Sverdrup, H. U., 1947: Wind-driven currents in a baroclinic ocean, with application to the equatorial currents of the eastern Pacific. *Proc. Natl. Acad. Sci. USA*, **33**, 318–326.
- Walker, A., and J. Pedlosky, 2002: On the instability of meridional baroclinic currents. *J. Phys. Oceanogr.*, **32**, 1075–1093.
- Wang, J., M. A. Spall, G. R. Flierl, and P. Malanotte-Rizzoli, 2012: A new mechanism for the generation of quasi-zonal jets in the ocean. *Geophys. Res. Lett.*, **39**, L10601, doi:10.1029/2012GL051861.
- Waterman, S., and S. R. Jayne, 2012: Eddy-driven recirculations from a localized transient forcing. *J. Phys. Oceanogr.*, **42**, 430–447.
- Xie, S.-P., W. T. Liu, Q. Liu, and M. Nonaka, 2001: Far-reaching effects of the Hawaiian Islands on the Pacific ocean-atmosphere system. *Science*, **292**, 2057–2060.
- Yoshida, S., B. Qiu, and P. Hacker, 2010: Wind-generated eddy characteristics in the lee of the island of Hawaii. *J. Geophys. Res.*, **115**, C03019, doi:10.1029/2009JC005417.
- , —, and —, 2011: Low-frequency eddy modulations in the Hawaiian Lee Countercurrent: Observations and connection to the Pacific decadal oscillation. *J. Geophys. Res.*, **116**, C12009, doi:10.1029/2011JC007286.
- Yu, Z., N. Maximenko, S.-P. Xie, and M. Nonaka, 2003: On the termination of the Hawaiian Lee Countercurrent. *Geophys. Res. Lett.*, **30**, 1215, doi:10.1029/2002GL016710.

Copyright of Journal of Physical Oceanography is the property of American Meteorological Society and its content may not be copied or emailed to multiple sites or posted to a listserv without the copyright holder's express written permission. However, users may print, download, or email articles for individual use.